EXPERIMENTELLE PHYSIK

Measurements with a Multi-Wire Proportional Chamber for Small Animal Positron Emission Tomography

Diplomarbeit
von
Don Vernekohl

Westfälische Wilhelms-Universität Münster
Institut für Kernphysik

— Februar 2010 —

Contents

CHAPTER I

Introduction

Positron Emission Tomography (PET) is an imaging modality used in nuclear medicine. Many research projects use PET on small animals like mice or rats to test pharmaceuticals, especially new tracers, or to research the development of special diseases. As organs of mice and rats are much smaller than those of humans, PET scanners for small animals have to deliver a high spatial resolution. Scintillation based detectors represent the vast majority of all PET scanners. A disadvantage of high resolution small animal scanners, based on scintillation detectors, is that they are very expensive and that they hardly reach a spatial resolution under one millimetre.
By the 1970's a PET scanner based on *Multi-Wire Proportional Chamber* (MWPC) technology was built which reached a spatial resolution of approximately one millimetre. Subsequently, the quadHIDAC emerged which is a commercially available PET scanner produced by Oxford Positron Systems.
The quadHIDAC is not under production anymore. I am part of a group which concentrates on the development of a new detector system based on MWPC technology.

The thesis is separated in two parts. The first four chapters focus the theoretical background to understand the basics of PET and to illuminate the physics behind the signal originating processes. It also details the technical construction of a prototype chamber.
The second part of this thesis details performance measurements of prototype chambers.

CHAPTER II

Basic Physical Principles

The first section of this chapter handles the β-decay, especially the β^+-decay, as it is the fundamental decay used for PET. The second and third section describe the principles of interaction between radiation and matter. The section for interaction of ionised particles with matter focuses especially on electrons and positrons as they are important particles in PET and for gas detectors.

II.1 β^+-Decay

II.1.1 Radioactive Radiation

Radioactive radiation is subdivided into three types of radiation: α-, β- and γ-radiation and these three types of radiation originate in the nucleus of an atom. α-radiation are ^4He nucleus which can be stopped easily with solid matter because of the high cross section of ^4He. γ-radiation is electromagnetic radiation. β-radiation consists of electrons or positrons. Today it is possible to produce synthetic radiation from many elements which are handled in heavy ion physics.

II.1.2 β-Decay

The energy spectrum of the α- and γ-decay is discrete, as the α-decay is a two particle decay and the γ-decay originates from discrete energy levels of the excited nucleus. The energy distribution of the β-decay, on the other hand, is continuous which stands against a two body decay because the energy conservation law is violated. Pauli predicted the existence of a new particle in 1931, since the momentum and angular momentum law were not consistent with a two body decay. The proof of the existence of the neutrino was done by Cowan and Reines in 1956. The determination of the exact mass of the neutrino is still the focus of present research projects. Nowadays the β-decay is described as a three particle decay and is distinguished into three different cases:

- **β^--decay**
  Inside of the nuclei a neutron decays into a proton. For charge conservation it emits an electron e^- and an electron anti-neutrino $\overline{\nu}_e$. The energy equation is described by
  $$^A_ZX \longrightarrow ^A_{Z+1} Y + e^- + \overline{\nu}_e + Q \tag{II.1}$$
  where X describes the mother nuclei, Y the daughter nuclei, and Q is the kinetic energy which is shared between the three particles. Also a free neutron can undergo a β^--decay as the neutron has a slightly higher mass than the proton.

- **β^+-decay**
  The β^+-decay occurs when a proton decays into a neutron. The proton itself is stable and can only decay if the mother nuclei is in an exited state.
  $$^A_ZX \longrightarrow ^A_{Z-1} Y + e^+ + \nu_e + Q \tag{II.2}$$

- **electron capture**
  If the mother nuclei cannot provide enough energy, it is possible that the nuclei captures an electron from the K-shell to initialize the conversion of a proton into a neutron.
  $$^A_ZX + e^- \longrightarrow ^A_{Z-1} Y + \nu_e + Q \tag{II.3}$$

II.2 Interaction of Electromagnetic Radiation with Matter

When electromagnetic radiation penetrates a piece of matter of the length x the intensity follows the exponential absorption law

$$I = I_0 e^{-\mu x} \tag{II.4}$$

where μ is the attenuation coefficient and I_0 the intensity of the initial radiation. It can be calculated with the total cross section σ with [BWW01]

$$\mu = \frac{\rho N_A}{A}\sigma \tag{II.5}$$

where N_A is the Avogadro constant and A the atomic number. The total cross section consists of different types of interaction $\sigma = \sigma_{ph} + \sigma_c + \sigma_{pair}$ where σ_{ph} stands for the cross section of the photo electric effect, σ_c for the cross section of the Compton effect, and σ_{pair} for the cross section of the pair production. Because pair production just occurs at energies over 1022 keV it is not that important for PET and will not be treated in this thesis.

II.2.1 Photo Electric Effect

In the photo electric effect the whole energy of the photon is transfered to a shell electron of the atom. The kinetic energy of the liberated electron is then

$$E_e = h\nu - E_B(e_j) \tag{II.6}$$

where $E_B(e_j)$ represents the binding energy of the electron in the $j = K, L, M$ shell of the atom. The photo electric effect is not allowed for free electrons because of momentum conservation so that the recoil energy has to be taken up from the whole atom. For photon energies higher than the binding energy of the K-shell electrons, photons are dominantly interacting with electrons from the K-shell.

The cross section for the photo electric effect in the K-shell is given in a non-relativistic approximation by [BWW01]

$$\sigma_{ph}^K = \left(\frac{32}{\varepsilon^7}\right)^{\frac{1}{2}} \alpha^4 Z^5 \sigma_{Th}^e \tag{II.7}$$

where $\varepsilon = E_\gamma / m_e c^2$ is the reduced photon energy and $\alpha = 1/137$ is the fine structure constant. The Thomson cross section for elastic scattering is given by

$$\sigma_{Th}^e = \frac{8}{3}\pi r_e^2 \tag{II.8}$$

The cross sections for the L- and M-shell electrons can also be calculated but are much more complex.

The ionised atom causes secondary radiation because the hole in the K-shell can be filled with an electron from the outer shells which causes secondary photons or Auger electrons.

II.2.2 Compton Scattering

The Compton effect is the elastic scattering of photons on quasi free electrons. The electrons in the atom shell can be treated as quasi free when the binding energy is negligible against the photon energy. If E_γ, $\mathbf{p}_\gamma$ are the energy and the momentum of the initial photon and E'_γ, $\mathbf{p}'_\gamma$ are the energy and the momentum after the collision the conservation laws can be described as follows

$$\begin{aligned} E_\gamma + m_e c^2 &= E'_\gamma + E_e \\ \mathbf{p}_\gamma &= \mathbf{p}'_\gamma + \mathbf{p_e} \end{aligned} \tag{II.9}$$

where E_e,$\mathbf{p_e}$ represent the energy and the momentum of the electron. It is assumed that the electron is not moving in the initial state. The photon momentum can be described by $\mathbf{p}_\gamma = \frac{\mathbf{E}_\gamma}{\mathbf{c}}\mathbf{n}$ where $\mathbf{n}$ is the unit vector for the photon direction. The angle ϑ between the initial and the final photon direction is then given by $\mathbf{n} \cdot \mathbf{n'} = \cos\vartheta$. By squaring the conservation laws one obtains

$$(E_\gamma - E'_\gamma)^2 + 2m_e c^2 (E_\gamma - E'_\gamma) + m_e^2 c^4 = E^2 \tag{II.10}$$

$$E_\gamma^2 - E_\gamma E'_\gamma \cos\vartheta + E'^2_\gamma = p^2 c^2 \tag{II.11}$$

The subtraction of Equation II.10 with Equation II.11 delivers

$$E_\gamma E'_\gamma (1 - \cos\vartheta) - m_e c^2 (E_\gamma - E'_\gamma) = 0 \tag{II.12}$$

One can solute Equation II.12 to obtain the energy of the escaping photon

$$E'_\gamma = \frac{E_\gamma}{\frac{E_\gamma}{m_e c^2}(1 - \cos\vartheta) + 1} \tag{II.13}$$

From Equation II.12 one can also derive the kinetic energy of the outgoing electron

$$T_e = E_e - mc^2 = E_\gamma - E'_\gamma = \frac{E'_\gamma E_\gamma}{m_e c^2}(1 - \cos\vartheta) \tag{II.14}$$

with II.13 and $E_\gamma = h\nu$ this becomes

$$T_e = h\nu \frac{\frac{h\nu}{m_e c^2}(1 - \cos\vartheta)}{\frac{h\nu}{m_e c^2}(1 - \cos\vartheta) + 1} \tag{II.15}$$

The total cross section per electron has been calculated the first time by Klein and Nishina [NK29]

$$\sigma_c^e = 2\pi r_e^2 \Big\{ \Big(\frac{1+\varepsilon}{\varepsilon^2} \Big) \Big[\frac{2(1+\varepsilon)}{1+2\varepsilon} - \frac{1}{\varepsilon} \ln(1+2\varepsilon) \Big] + \frac{1}{2\varepsilon} \ln(1+2\varepsilon) - \frac{1+3\varepsilon}{(1+2\varepsilon)^2} \Big\} \tag{II.16}$$

so that one gets the total cross section for Compton scattering for an element with atomic number Z with

$$\sigma_c = Z \sigma_c^e \tag{II.17}$$

II.3 Interaction of Ionised Particles with Matter

Interaction of ionised particles, e.g. protons or electrons, with matter is different to the interaction of photons with matter. The intensity of a beam of ionised particles does not follow the absorption law Equation II.4. Ionised particles diminish their kinetic energy discrete via inelastic scattering with the electrons in the atom shell or via elastic scattering with the nucleus. This is in first approximation true for particles which interact over the electromagnetic force and are heavier than electrons. The energy loss per path length x has been derived by Bethe and Bloch from quantum electrodynamics [Leo87]

$$-\frac{dE}{dx} = 2\pi N_a r_e^2 m_e c^2 \rho \frac{Z}{A}\frac{z^2}{\beta^2}\left[ln\left(\frac{2m_e\gamma^2 v^2 W_{max}}{I^2}\right) - 2\beta^2\right] \tag{II.18}$$

with

r_e: classical electron radius

Z: atomic number of absorbing material

A: atomic weight of absorbing material

I: mean excitation potential

m_e: electron mass

N_a: Avogadro's number

ρ: density of absorbing material

z: charge of incident particle in units of e

W_{max}: maximum energy transfer in a single collision

$\beta = v/c$ of the incident particle

$\gamma = 1/\sqrt{1-\beta^2}$

The maximum energy transfer W_{max} occurs at a head-on collision. For an incident particle of mass M, kinematics give

$$W_{max} = \frac{2m_e c^2\eta^2}{1 + 2s\sqrt{1+\eta^2} + s^2} \tag{II.19}$$

where $s = m_e/M$ and $\eta = \beta\gamma$. As it is difficult to calculate the mean excitation potential theoretically semi-empirical formulas have been deduced from measurements. One such formula is

$$\begin{aligned} \frac{I}{Z} &= 12 + \frac{7}{Z}\ \text{eV} && Z < 13 \\ \frac{I}{Z} &= 9.76 + 58.8Z^{-1.19}\ \text{eV} && Z \geq 13\ . \end{aligned} \tag{II.20}$$

There are also more types of energy loss than elastic and inelastic scattering. The occurrence of emission of Cherenkov radiation, nuclear reactions, and Bremsstrahlung also originate an energy loss. However, Cherenkov radiation and Bremsstrahlung only occurs at relativistic velocities and nuclear reactions require appropriate targets.

For the energy loss of electrons and positrons the Bethe-Bloch-Formula Equation II.18 has to be modified in the way that the assumption of the incident particle remaining undeflected during the collision is invalid. The collision is also between identical particles, so that the calculation must take into account their indistinguishability. The energy loss then becomes [Leo87]

$$-\frac{dE}{dx} = 2\pi N_a r_e^2 m_e c^2 \rho \frac{Z}{A}\frac{1}{\beta^2}\left[ln\frac{\tau^2(\tau+2)}{2(I/m_e c^2)^2} + F(\tau)\right] \tag{II.21}$$

where τ is the kinetic energy of the incoming particle in units of $m_e c^2$. $F(\tau)$ differs for electrons and positrons:

$$\begin{aligned} F(\tau) &= 1 - \beta^2 + \frac{\frac{\tau^2}{8} - (2r+1)\ln 2}{(\tau+1)^2} && \text{for } e^- \\ F(\tau) &= 2\ln 2 - \frac{\beta^2}{12}\left(23 + \frac{14}{\tau+2} + \frac{10}{(\tau+2)^2} + \frac{4}{(\tau+2)^3}\right) && \text{for } e^+ \end{aligned}$$

The remaining quantities are as described previously in Equation II.18.

Additionally there can be made *shell-* and *density- corrections* to the formulas Equation II.18 and Equation II.21. For detailed information the reader may refer to [Leo87].

CHAPTER III

PET

As PET should be the application for our intended scanner, this chapter gives the basic issues which are necessary to understand PET. The first section describes functional imaging modalities which are used in nuclear medicine. After the principle of PET will be described, the following sections will give some details on the radionuclides which can be used in PET and how they influence the limits of spatial resolution. Other spatial resolution limiting factors in PET are the detection principle itself and noncolinearity in the annihilation process. The last section intends to give first insights in the wide field of image reconstruction in PET.

III.1 Functional Imaging Modalities in Nuclear Medicine

The aim of functional imaging is to visualize the metabolism of specific molecules in vivo. To be able to determine where a specific molecule migrates within the organism, a radioactive atom is added to this molecule. The labeled molecule is called *tracer* and should undergo the same metabolism as the unlabeled equivalent. When the labeled atom within the molecule decays, it is possible to determine its position. In nuclear medicine there are three different devices available which are able to detect the photons from the radioactive decay. The easiest way to obtain a functional image is to make a planar scintigram with a gamma camera. The image reconstruction of planar scintigraphy is closely related to X-ray photography.

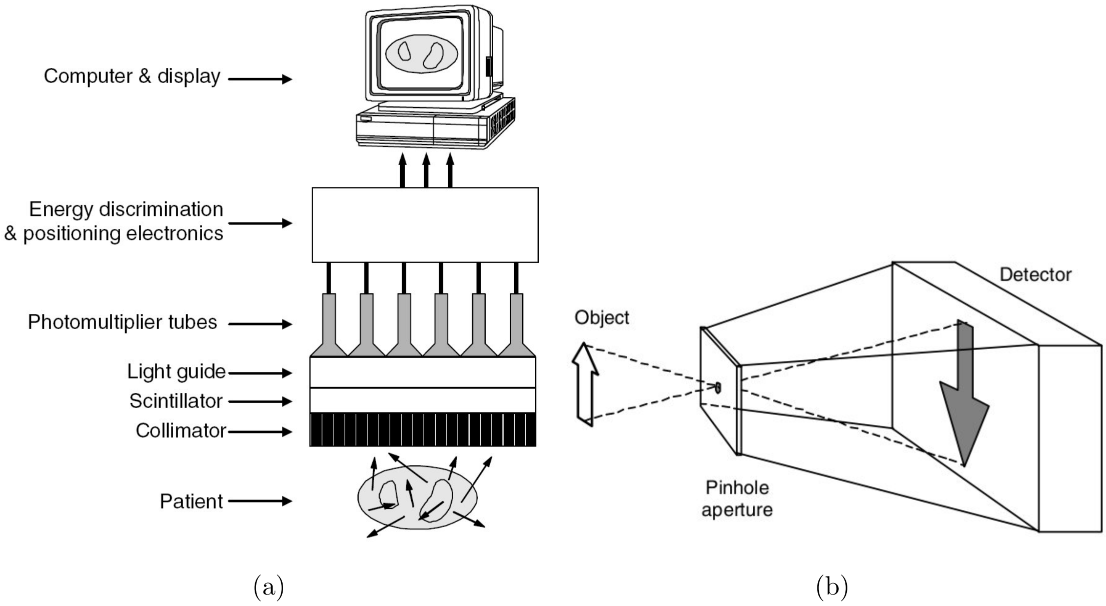

(a) (b)

Figure III.1: Principle of a gamma camera (a). Sketch of a pinhole camera (b) [WA04]

The single photons from the radioactive decay of the tracer are detected with a scintillation crystal. The position of the interaction of the photon with the crystal is commonly determined with an array of photo multiplier tubes. The possible directions of the photons can be restricted by using a collimator in front of the detector. The collimator can be realized with various geometric shapes and it is also possible to construct pin-hole gamma cameras if the imaged object is close to the pinhole. Figure III.1 shows a sketch of a simple gamma camera and the principle of a pin-hole gamma camera.

The other two devices are summarized to **E**mission **T**omography. The term *emission tomography* is a marriage of two basic principles: imaging through the use of gamma-ray *emission* (called the tracer principle) and volumetric imaging of the body's interior (called *tomography*) [WA04].

In *single-photon emission computed tomography* (SPECT), one gamma camera is rotated or several gamma cameras are positioned around the imaged object to obtain two-dimensional slice images or three-dimensional volume images.

SPECT and PET are non competing devices. It depends on the tracer which modality is used. Where SPECT is in principle able to use every tracer, PET is restricted to tracers which are labeled with radionuclides which undergo a β^+-decay.

This means that a PET tracer can be used in a SPECT scanner, but the sensitivity drops significantly due to the collimator which is not needed in PET scanners.

An advancement of SPECT scanners is the ability to use different tracers with different decay energies at the same time.

III.2 Principle of PET

A PET examination uses tracers where a radionuclide is added which undergoes a β^{+}-decay. The liberated positron loses energy due to collisions with the ambient matter. In tissue the positron comes to rest within a few millimetres and within a nanosecond. Near or at the point at which the positron stops the probability to combine with a free electron is high. The bounded state called *positronium* has a short lifetime and decays most probably into two photons which are emitted back to back. By measuring these two photons a line is defined where the positronium decay has taken place. This line is called *line of response* (LOR). With an appropriate number of LORs it is possible to reconstruct a PET image of the tracer distribution. Figure III.2 illustrates these processes.

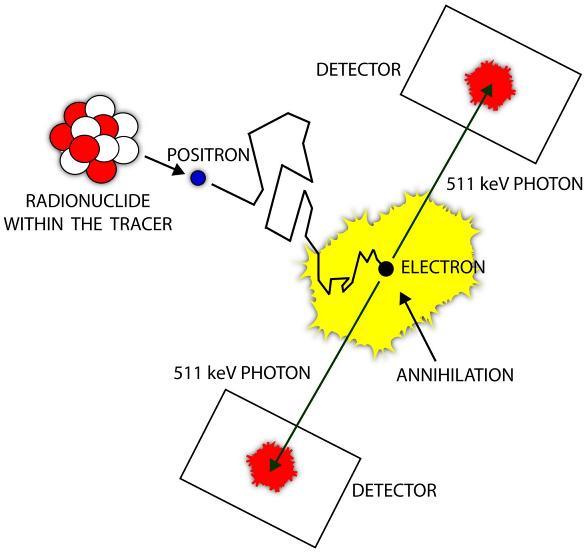

Figure III.2: Scheme of the process of positron emission and subsequent positron-electron annihilation. The annihilation results in the emission of two 511 keV photons. These photons are detected by a PET scanner.

III.3 Radionuclides

Many radionuclides are applicable in nuclear medicine. There are several requirements for a radionuclide for each application: radioactive half-life, available techniques to add the radionuclide to the tracer molecule, energies of the emitted photons or positrons and others. The half-life value is very important because on the one hand it has to be long enough, so that the tracer has enough activity after the fabrication process. On the other hand it is not good if the half-life value is too long in order that the acquisition time to take the image should be short.

The available techniques to add a radionuclide to the desired molecule are limiting the number of useful radionuclides for each application. Many chemical investigations are motivated by improving these techniques or finding new techniques.

The energies of the photons for SPECT scanners have to be appropriate to the object that should be imaged and the applied scanner. On the one hand for low energy photons the probability to undergo interaction within the body is too high, therefore, the measured photon is not correlated to the position of the tracer. On the other hand photons with too much energy cannot be well collimated.

The positron energy is a limiting factor for the reachable spatial resolution of a PET image. In Figure III.3 (a) the decay scheme of four common β^+-emitters which are applicable for PET are presented.

The β-energy spectrum is of the form (Wu and Moskowski, 1966):

$$N(E)dE = gF(Z,E)pE(E_{max} - E)^2 dE \tag{III.1}$$

where $N(E)$ is the number of decays at β energy E, E_{max} is the maximum energy in units of mc^2, p is the momentum of the β particle in units of mc, g is the weak coupling constant, $F(Z,E)$ is the Fermi function, and Z is the atomic number of the daughter nucleus. In the Fermi function the coulomb interaction of the β with the daughter nucleus is considered. The coulomb field decelerates electrons and accelerates positrons. A non-relativistic approximation for $F(Z,E)$, valid for allowed transitions of lighter elements (Wu 1966; Daniel 1968) is:

$$F_{allowed}(Z,E) = 2\pi\eta/(1 - e^{-2\pi\eta}) \tag{III.2}$$

with $\eta = \pm Z\alpha E/p$ where α is the fine structure constant. The energy spectras for the β^+-emitters are plotted in Figure III.3(b).

The distance from the position of decay and point of annihilation that the positron covers is correlated to the energy of the positron.

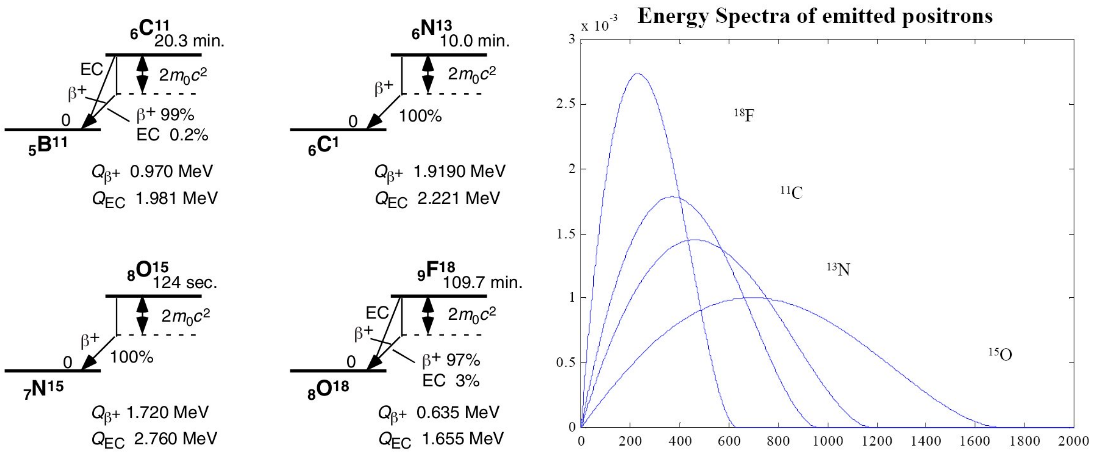

(a) (b)

Figure III.3: Decay schemes of common β^+-emitters. $Q_{\beta+}$ and Q_{EC} represent the total energy available to positron and electron capture decays, respectively. The maximum available energy for β^+-decay is the full transition energy from parent to daughter minus twice the electron rest mass (1.022 MeV) (a)[WA04]. Energy spectra of these positron emitters (b)[Smi99]

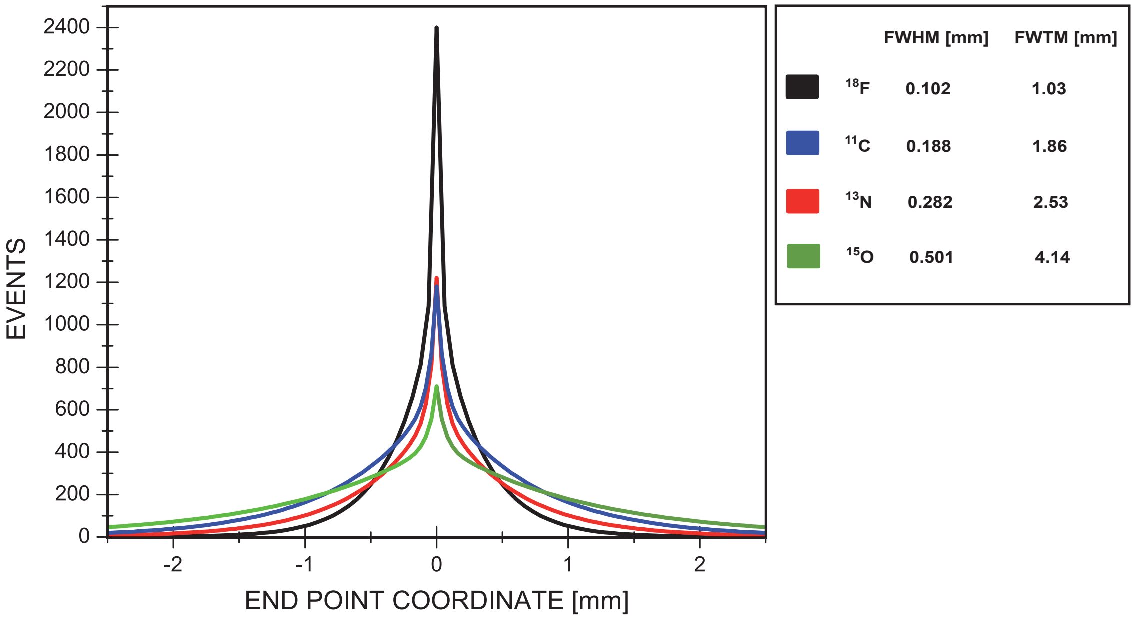

Figure III.4: Simulations of the positron range in water for different β^+-emitters in water[LH99].

Levin and Hoffmann made Monte-Carlo simulations of the positron migration with the common β^+-emitters in water [LH99] for 100,000 decays. Figure III.4 shows fit functions from histograms of the x coordinate of the positron end point distribution from the simulations with the associated FWHM[1] and FWTM[2].

So far these simulations have not been approved experimentally. Experiments deliver different mean ranges between one and three millimetres for the different isotopes. A detailed comparison between the experimental data and the simulations is presented in the diploma thesis of H.Huenteler [Hü07]. A simulation of the positron range of ^{18}F has also been made by [Got10], shown in Figure III.5, where the mean range is 475 μm with a RMS[3] of 377 μm. These values fit better to the experimental data than the simulations by Levin and Hoffmann [LH99].

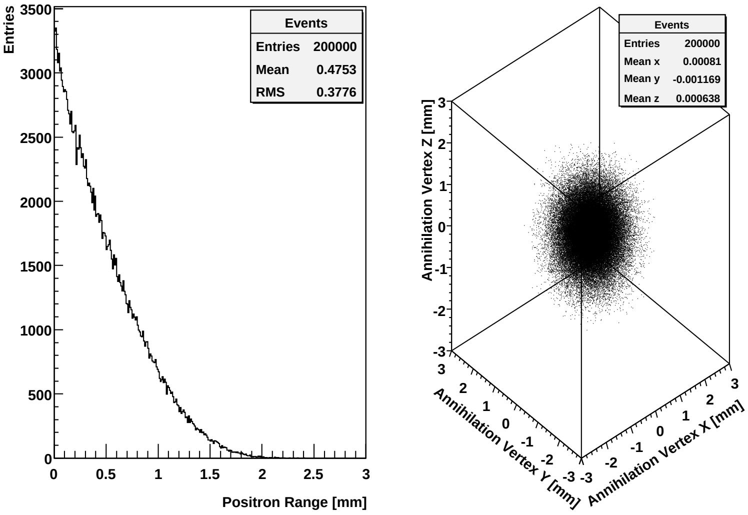

Figure III.5: Simulations of the positron range in water for ^{18}F [Got10].

As the positron range is a limiting factor for spatial resolution, it would be desirable to apply strong magnetic fields to diminish the positron range. In the linear magnetic field of a MRT the positron range would be diminished in two dimensions perpendicular to the magnetic field. Recently it has become possible to combine PET and MRT due to development of *avalanche photo diodes* (APDs) which re-

---

[1] FWHM = Full width at half maximum

[2] FWTM = Full width at tenth maximum

[3] RMS = root mean square

place the photo multiplier tubes (PMTs) within scintillation based scanners. These PMTs cannot be used in strong magnetic fields [Sch09].

III.4 Coincidence Detection

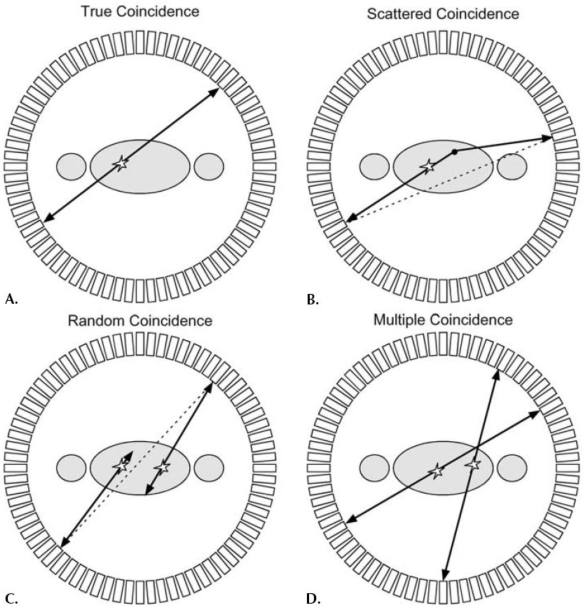

Figure III.6: The four main coincidence event types. A: Both annihilation photons escape the body and are detected. B: One or both of the two annihilation photons interacts in the body prior to detection. C: A coincidence is generated by two photons originating from two separate annihilations. D: Three or more photons are detected simultaneously[CD06].

If a PET scanner detects two signals within a time window, a LOR can be defined. All coincidences whose LORs cross the point of annihilation are called *true* coincidences.

There are also types of coincidences whose LORs do not cross the point of annihilation. The annihilation photons can undergo Compton scattering within the imaged object or the scanner apparatus before being detected. These are called *scattered* coincidences. It is possible to reject them due to the fact that the scattered photons have a lower energy than the unscattered. Typical PET scanners use an energy window from 350 keV to 650 keV due to limited energy resolution. Hence, only scattered photons with large scattering angles can be rejected.

As a photon moves with speed of light, it takes around 30 ns for 10 cm.

Therefore, the time window to detect two photons has to be appropriate to the size of the scanner and the dedicated *field of view* (FOV). Detectors are also limited in time resolution. Scintillation crystals for example have a time resolution in the order of some nano seconds[CD06]. That is because the distance from the PMT or APD to the position where the scintillation photons arise is varying and scintillation decay has statistical fluctuations. Therefore, a time window is necessary to decide if two signals originate from one annihilation or not. This, of course, causes wrong decisions especially if a high activity has been administered to the imaged object. There are two types of accidental coincidences which are correlated to the time window. On the one hand there are the *random* coincidences where two photons from different decays are detected. The detection rate of random coincidences N_R is correlated to the detection rate of the given detectors N_1 and N_2 and the gating time τ by:

$$N_R = 2\tau N_1 N_2 \tag{III.3}$$

On the other hand there are *multiple* coincidences where more than two photons are detected. Because there are several LORs possible, these coincidences are rejected by the detector electronics. Figure III.6 illustrates the different types of coincidences.

III.5 Positron Annihilation and Noncolinearity

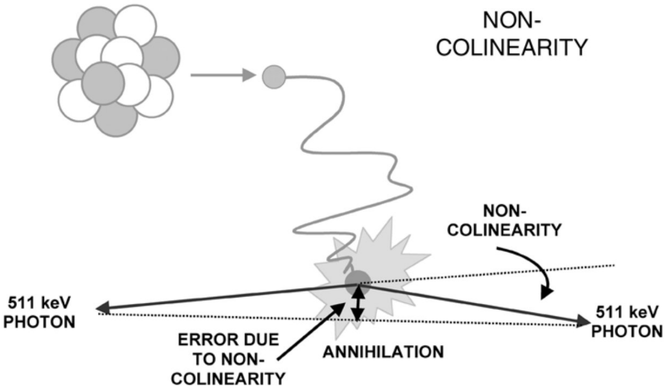

Figure III.7: Influence of the noncolinearity to the determination of the LOR [CD06].

The processes of positron annihilation is a little more complex as depicted in the introduction of this chapter. There are some annihilation routes for the positron. First it is possible for the positron to decay within the flight before reaching thermal equilibrium. But the fraction of positrons which annihilate in-flight is just around 2% [Hei53].

All other positrons reach thermal equilibrium. The strong coulomb field of the nucleus permits the positrons to get close to electrons of the inner shells of the atoms. Therefore, the positrons combine with free electrons, weakly bound electrons of the outer shells or at places of low electric potential between two atoms within a molecule.

Depending on the spin configuration, the positron and the electron can form the singulet ^{1}S configuration called *parapositronium* or the triplet ^{3}S configuration called *orthopositronium*. Parapositronium decays most frequently in two photons due to angular momentum law. The half-life value is[MRRS85]:

$$\tau_{2\gamma} = 1.25 \times 10^{-10} n^3 \mathrm{s} \tag{III.4}$$

where n is the main quantum number. Orthopositronium has a spin of one and, therefore, it decays at least in three photons. It is more stable and the half-life value is:

$$\tau_{3\gamma} = 1.40 \times 10^{-7} n^3 \mathrm{s} \tag{III.5}$$

The binding energy of positronium in the ground state is $E = 6,8$ eV which is half the binding energy of the hydrogen ground-state. If the positronium is built up in an excited state it will decay fast to the ground state. The annihilation of an excited state is possible but unlikely.

The ratio of the cross sections for building para- or orthopositronium is [MRRS85]:

$$\frac{\sigma_{2\gamma}}{\sigma_{3\gamma}} = 372 \tag{III.6}$$

Hence, parapositronium annihilation is the dominating process.

The centre of mass of the positronium is not exactly at rest, even if the positron reaches thermal equilibrium. The additional energy from the binding energy and the moving centre of mass is in the order of $E \approx 10$ eV and is responsible for noncolinearity. Noncolinearity means that the angle between the two photons is not exactly 180° and the photons do not have an exact energy of 511 keV. This causes a mispositioned LOR as depicted in Figure III.7. The angular deviation from 180° is about ±0.25°[CD06].

III.6 Image Reconstruction

The tracer distribution within the imaged object can be interpreted as a density function:

$$f \; : \; \mathbb{R}^N \; \rightarrow \; \mathbb{R}^+ \qquad N = 2, 3 \tag{III.7}$$

The ring geometry of commonly used PET and CT scanners delivers the possibility of obtaining 2D datasets from a 3D object. Traditionally the 2D data set is stored in a *sinogram* matrix $s(r, \Phi)$ where the Cartesian coordinates are transformed to polar coordinates r and Φ. Therefore, each element within the sinogram represents one line of response L_i. The tracer distribution is correlated to this number by:

$$\int_{L_i} f(\mathbf{x}) dx_l \approx s_i \tag{III.8}$$

There are two different approaches to reconstruct the sought-after tracer distribution f out of the measurements s.

III.6.1 Filtered Back Projection

The first method is rather analytical and is called *filtered back projection* FBP. It can be viewed as a numerical implementation of the inverse *Radon Transformation.* Prior to the back projection step the data is filtered to suppress artefacts.

A projection in 2D is the integration along all LORs at a fixed angle Φ and, therefore, is represented by one row within the sinogram.

Hence, each point of the back projection $b(x, y)$ is defined by the integral of the projection of this point over all angles :

$$b(x, y) = \int_0^\pi p(r, \Phi) d\Phi \tag{III.9}$$

with $r = x \cos \Phi + y \sin \Phi$. As the information where the annihilation along the LOR has taken place is lost by the integration in Equation III.8, the simple back projection is blurred by the system response function:

$$h(x, y) = \frac{1}{\sqrt{x^2 + y^2}} \tag{III.10}$$

This blurring artefact can be filtered in Fourier space with a filter function $|v_r|$ so that the tracer distribution is given by:

$$f(x, y) = \int_0^\pi p^F(r, \Phi) d\Phi \tag{III.11}$$

where the filtered projection is given by:

$$p^F(r, \Phi) = F^{-1}\{|v_r| \times F\{p(r, \Phi)\}\} \tag{III.12}$$

Here we see that FBP is an analytical procedure but as the sinogram delivers binned data instead of a projection function, following algorithm is used for pixel driven FBP [CD06]:

$$f(x, y) = \frac{1}{N} \sum_{n=1}^{N} s^*(r, \Phi_n) \tag{III.13}$$

where the filtered projection is given by:

$$s^*(r, \Phi) = F^{-1}\{|v_r| \times F\{s(r, \Phi)\}\} \tag{III.14}$$

Here $f(x, y)$ is divided into pixels where for each pixel and each angle the sinogram coordinate r has to be calculated with $r = x \cos \Phi_n + y \cos \Phi_n$. The calculated value of r will normally not fall exactly to a sinogram element, therefore, linear interpolations have to be used to determine the pixel content.
For FBP the 3D image reconstruction is also possible, but the mathematics are more complex.

III.6.2 Iterative Image Reconstruction

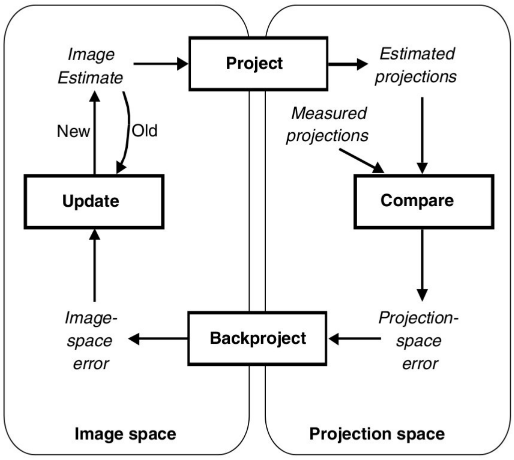

Figure III.8: Flowchart of a generic iterative reconstruction algorithm [WA04].

Next to the analytical approaches there are the iterative image reconstruction methods. First a grid is arranged over the designated *field of view* (FOV).

Then the tracer distribution is estimated by filling the pixels(2D) or voxels(3D) of the grid[4] with appropriate values f_j, where $j = 1, ..., N$ signs each pixel (voxel). Now it is desired to make a projection of this tracer distribution. This is made with a matrix **H** which contains the response of each pixel for every possible LOR. **H** can be constructed also for complicated imaging systems. Therefore, a discrete number of projections ($i = 1, ..., M$), of the estimated tracer distribution can be calculated with

$$\mathbf{s} = \mathbf{H}\mathbf{f} \quad . \tag{III.15}$$

The estimated projections can be compared with the measured projections. The projection-space error which can be created out of the comparison is then back projected to yield an error in image-space. This error can be used to make a tracer distribution estimation. A scheme of this procedure is illustrated in Figure III.8.

An established representation of such an iterative algorithm is the *expectation maximization* (EM) algorithm. The EM algorithm is derived with the *maximum likelihood* (ML) method and with the consideration that the radioactive decay and the detection of radiation are Poisson distributed. One possible expression of this algorithm is given by[WA04]:

$$f_j^{n+1} = \frac{f_j^n}{\sum\limits_{i'} h_{i'j}} \sum_i h_{ij} \frac{s_i}{\sum\limits_k h_{ik} f_k^n} \tag{III.16}$$

As described, this algorithm can be implemented to derive 2D or 3D images, even though the 3D image processing requires substantially greater computation time.

In the past FBP was generally used for image reconstruction because of limitations in computational performance. Nowadays this is no longer a limitation, but there is not yet a consensus that iterative reconstructions are always superior to FBP images or, at least, that the benefits of iterative reconstruction always justify the increased computational costs; therefore, the two approaches will probably continue to coexist for some time[WA04].

It should be mentioned that this paragraph just maps a few points of the wide field of image reconstruction. A good introduction to this field is given by [WA04] and the more advanced reader may be referred to [Nat86].

---

[4] If no prior information of the object is given, it is filled with zeros.

CHAPTER IV

Gas Detectors

Since the first radiation detector has been utilized, numerous principles for detection with different characteristics have been involved. Because of the vast number of applications where radiation detectors are used, the aim of research has been and still is the improvement of individual detector properties and to push the different advantages of each detector principle to their physical limits. These detector properties could be e.g. energy resolution, spatial resolution, sensitivity, dead time, saturation or the feature to detect just a special kind of radiation. This chapter focuses on gaseous detectors, especially on the signal developing processes within the counter tube, to introduce the basic principles necessary to understand a *multi-wire proportional chamber* (MWPC), which will be the topic of the next chapter. The MWPC is the fundamental detector principle for our intended PET scanner.

IV.1 Ionisation Chamber

A simple way to construct a gas detector is to fill a plate capacitor with gas. Radiation which enters the detector ionises or excites gas molecules. While ionisation directly creates ion pairs which are needed to produce a signal, excited molecules can also result in ion pairs, for example if the de-excitation liberates an electron which is called delta-ray or if the excited molecule ionises a second atom in a collision which is called Penning-effect. A detailed overview of ionisation processes is given by Leo [Leo87]. A voltage, which has to be high enough to prevent the ion pairs of recombination, is applied to the capacitor, so that the ion pairs will move to the electrodes. The moving charges induce a signal in the electrodes.

IV.2 Counter Tube

Similar to the Ionisation chamber, described before, a counter tube is a gas filled capacitor, but in this case it is a cylindrical capacitor which creates an inhomogeneous electric field. The capacitor can be described by two coaxial cylinders Figure IV.1 where the inner cylinder is realised as a thin wire in the middle of the capacitor which is put on a positive potential.

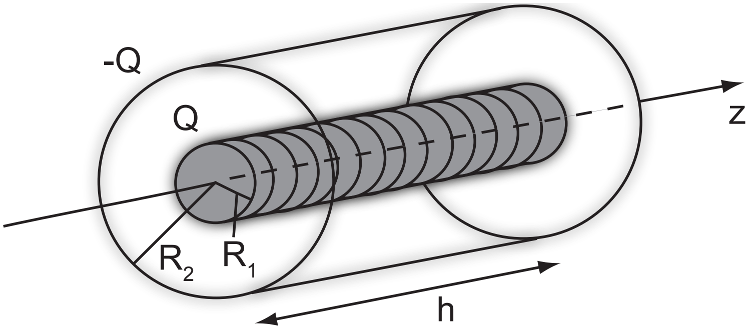

Figure IV.1: Cylindrical capacitor [Nol89]

IV.2.1 Electric Field

The electric field within the capacitor can be obtained by calculating the flux through the surface of a further coaxial cylinder $d\mathbf{f} = (\rho d\varphi dz)\mathbf{e}_\rho$ [1]. With cylinder coordinates $\mathbf{r} = (\rho, \varphi, z)$ and the physical Gaussian law[2] one obtains [Nol89]:

$$\int_S \mathbf{E} d\mathbf{f} = \rho E(\rho) 2\pi h = \frac{1}{\epsilon_0} \int_V \rho(r') d^3 r' = \begin{cases} \frac{1}{\epsilon_0} Q & \text{for } R_1 < \rho < R_2 \\ 0 & \text{else} \end{cases}$$

---

[1] The flux through the face is zero because $d\mathbf{E}$ and $d\mathbf{f}$ are perpendicular.

[2] The physical Gaussian law says that the flux of the electric field through a surface of a volume V is equal to the overall charge within V [Nol89].

So one gets for the electrical field within the capacitor

$$\mathbf{E}(\mathbf{r}) = \frac{Q}{2\pi\epsilon_0 h\rho}\mathbf{e}_\rho \quad . \tag{IV.1}$$

The integration with maintaining the boundary conditions yields

$$\varphi(\mathbf{r}) = \frac{Q}{2\pi\epsilon_0 h}\ln\frac{R_2}{\rho} \quad . \tag{IV.2}$$

Due to this potential, the voltage between the cylinders is

$$U = \frac{Q}{2\pi\epsilon_0 h}\ln\frac{R_2}{R_1} \quad . \tag{IV.3}$$

In order to $C = Q/U$ the capacitance of the counter tube is

$$C = \frac{2\pi\epsilon_0 h}{\ln\frac{R_2}{R_1}} \quad . \tag{IV.4}$$

IV.2.2 Operating Modes

For low electric fields the counter tube works as an ionisation chamber but if the electric field delivers sufficient energy to the electrons they cause further ionisations. The electrons from the ionisations are also accelerated by the electric field which cause further ionisations. This cascade effect results in an avalanche (for details see next paragraph). The pulse height generated by the avalanches is proportional to the number of primary ionisations and thus proportional to the energy of the impinging radiation. Due to this proportionality, this operating mode of the counter tube is called proportional counter. Figure IV.2 shows the different operating modes of the counter tube for α- and β- radiation. Operating modes for voltages beyond the proportional region will be described in Paragraph IV.2.6.

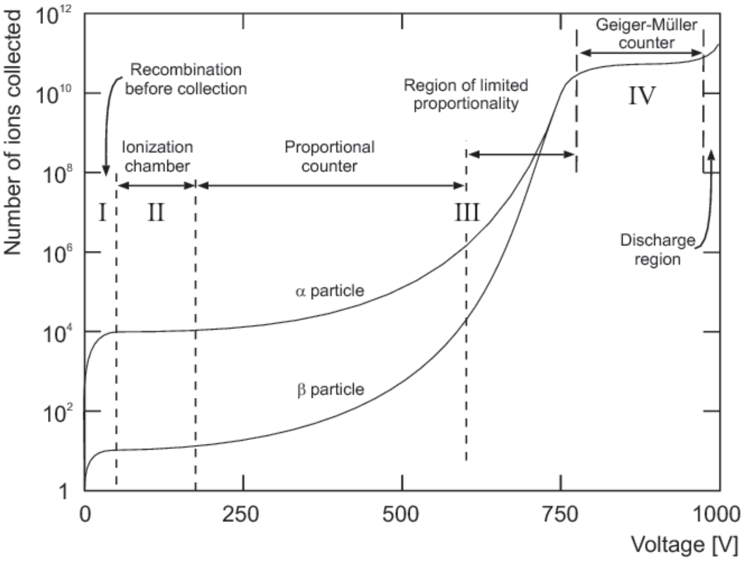

Figure IV.2: Number of ions collected as function of the applied voltage in a counter tube, showing the different regions of operation [Mel66].

IV.2.3 Avalanche Multiplication

According to Equation IV.1 the electric field has a $1/\rho$ proportionality which denotes that the electric field is relatively weak for large ρ, but becomes intense very close to the surface of the anode wire, so that the electrons which are produced from the impinging radiation are accelerated to the wire. Far away from the anode the electrons do not cause secondary ionisation and just drift to the anode, but close to the wire (a few wire diameters [Leo87]) the electrons gain enough energy to cause secondary ionisation, so that an avalanche is produced around the wire. Figure IV.3 shows the details of the formation process of the avalanche. The multiplication factor or *gas gain* is known as the number of created electrons n through the number of primary electrons n_0 and for a homogeneous field the gas gain is given by

$$M = \frac{n}{n_0} = e^{\alpha x} \tag{IV.5}$$

where α is known as the first Townsend coefficient, which is the reciprocal of the mean free path for the electrons for a secondary ionizing collision λ, and x is the path. For the inhomogeneous field of the counter tube Equation IV.1 the Townsend coefficient is a function of the path and thus the gas gain becomes [Kle92]

$$M = \frac{n}{n_0} = e^{\int \alpha(x) dx} \quad . \tag{IV.6}$$

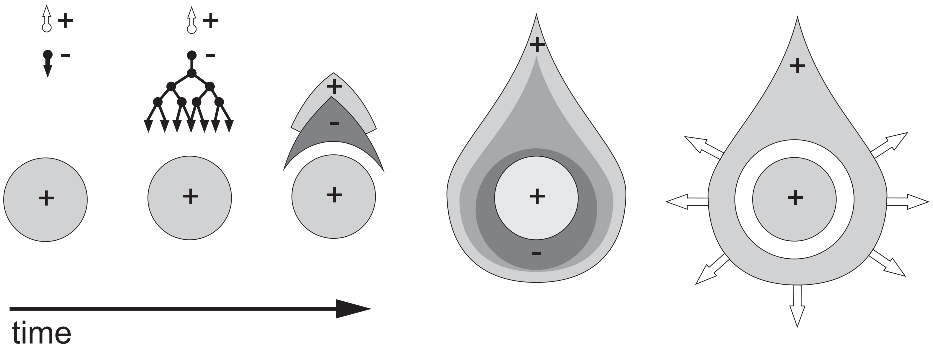

Figure IV.3: Time development of an avalanche in a proportional counter [Cha72]. A single primary electron proceeds towards the anode, in regions of increasingly higher fields, experiencing ionizing collisions; due to the lateral diffusion, a drop-like avalanche, surrounding the wire, develops. Electrons are collected in a very short time (around one ns) and a cloud of positive ions is left, slowly migrating towards the cathode.

The Townsend coefficient can be calculated with $\alpha = \sigma_i N$, where $N = 2.69 \times 10^{19}$ atoms/cm^3 is the atom density for noble gases. The collision ionisation cross section σ_i can be obtained by Figure IV.4. As the cross section grows with the electron energy Figure IV.4(a), one understands that the first Townsend coefficient grows with an increasing electric field Figure IV.4(b). For lower electric field intensities α follows an exponential distribution (b), which has been proposed by Townsend, but for higher electric field intensities this simple approximation is insufficient Figure IV.4(b). In the case of the lower electric field intensities α is proportional to the electron energy ϵ (compare Figure IV.4 (a) and (b))

$$\alpha = kN\epsilon \quad . \tag{IV.7}$$

As $1/\alpha$ is the mean free path for ionisation, the average energy ϵ of an electron from the electric field between collisions is E/α. With Equation IV.1 one gets

$$\alpha(\rho) = \sqrt{kNE} = \sqrt{\frac{kNCV_0}{2\pi\epsilon_0\rho}} \quad . \tag{IV.8}$$

With this expression the integral in Equation IV.6 can be solved and the gas gain can be calculated. Experimental data is in excellent agreement with this description for the counter tube with moderate gains. Detailed solutions for the integrals and comparisons to experimental data are given by [Sau77, Kor46].

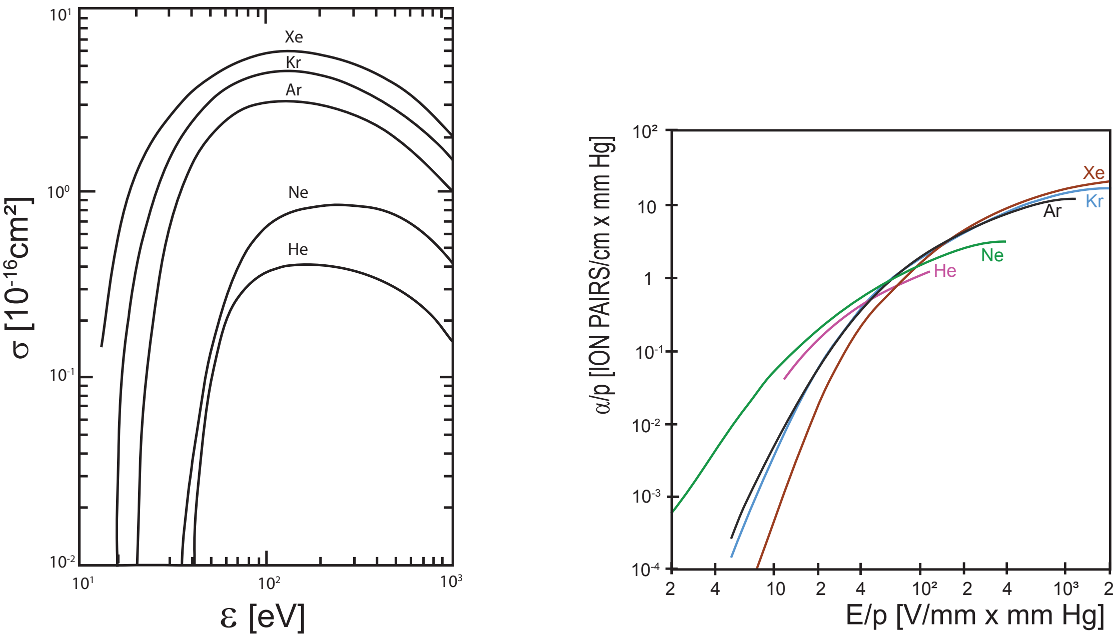

Figure IV.4: (a) Collision ionisation cross section σ_i as function of the electron energy ϵ for noble gases [All69]. (b) First Townsend coefficient as a function of the reduced electric field for noble gases [Bro59].

IV.2.4 Pulse Height of the Signals

To obtain the pulse height of a counter tube signal, we look at the energy conservation for a moving particle with the charge q within a capacitor first:

$$\frac{1}{2}CU^2 = \frac{1}{2}CU_0^2 - \int_{r_1}^{r_2} qE(\mathbf{r})dr \tag{IV.9}$$

where U is the voltage for the whole system and U_0 is the applied voltage. With the electric field of the counter tube taken from Equation IV.1 and $\Delta U = U - U_0$ with the assumption of $\Delta U \ll U_0$, we get

$$\begin{aligned} \frac{1}{2}C2U_0\Delta U &= -\int_{\rho_1}^{\rho_2} qE(\rho)d\rho = -\frac{qU_0}{\ln(R_2/R_1)}\ln\left(\frac{\rho_2}{\rho_1}\right) \\ \Delta U &= -\frac{q}{C\ln(R_2/R_1)}\ln\left(\frac{\rho_2}{\rho_1}\right) = -\frac{q}{2\pi\epsilon_0 h}\ln\left(\frac{\rho_2}{\rho_1}\right). \end{aligned} \tag{IV.10}$$

One can assume that all ions are created at the focal point of the avalanche ρ_0, which is close to the anode wire. By estimating that there are $N = nM$ electrons and ions (n is the number of primary ionisations and M the gas gain), the pulse height for the electrons becomes

$$\Delta U^- = -\frac{Nq}{2\pi\epsilon_0 h}\ln\left(\frac{\rho_0}{R1}\right) \tag{IV.11}$$

and for the ions

$$\Delta U^+ = -\frac{Nq}{2\pi\epsilon_0 h}\ln\left(\frac{R_2}{\rho_0}\right) \quad . \tag{IV.12}$$

Thus, the total maximum voltage is

$$U = \Delta U^+ + \Delta U^- = -\frac{Nq}{2\pi\epsilon_0 h}\ln\left(\frac{R_2}{R_1}\right) = -\frac{Nq}{C} \quad . \tag{IV.13}$$

One can also calculate the ratio of the two contributions

$$\frac{\Delta U^-}{\Delta U^+} = \ln\left(\frac{\rho_0}{R_1}\right)/\ln\left(\frac{R_2}{\rho_0}\right) \quad . \tag{IV.14}$$

If we approximate parameters for the counter tube which fit to our MWPC prototype with $R_2 = 1$ mm, $R_1 = 20\ \mu$m, and $\rho_0 \approx 22\ \mu$m we get a contribution of 2.5% for the electrons. For typical counter tube geometries operating in the proportional mode the electron contribution is between 1% and 4% [Leo87, Kle92][3].

IV.2.5 Time Development of the Signal

The main contribution to the time development is due to the ions as the electrons are collected by the anode wire within one ns. Electrostatic considerations show that if a charge q is moved by dr, in a system of capacitance C, the induced signal is

$$du = \frac{q}{CU_0}\frac{d\varphi}{dr}dr \quad .$$

Assuming that there are N positive ions created at the surface of the anode with constant mobility, integration yields

$$U(t) = -\int_0^t du = \frac{Nq}{2\pi\epsilon_0 h}\ln(\frac{r(t)}{R_1}) \quad . \tag{IV.15}$$

With the drift velocity for ions and Equation IV.1 it follows that

$$\frac{dr}{dt} = \mu^+\frac{E}{P} = \frac{\mu^+ CU_0}{2\pi\epsilon_0 hPr}$$

---

[3] For the ionisation chamber mode the contribution of electrons exceeds the contribution of the ions.

and therefore

$$\int_{R_1}^{r} r dr = \frac{\mu^+ C U_0}{2\pi\epsilon_0 h P}\int_0^t dt \qquad \text{or} \qquad r(t) = \left(R_1^2 + \frac{\mu^+ C U_0}{\pi\epsilon_0 h P} t\right)^{\frac{1}{2}} \quad . \tag{IV.16}$$

Substituting in Equation IV.15 one gets:

$$U(t) = -\frac{Nq}{4\pi\epsilon_0 h}\ln\left(1 + \frac{\mu^+ C U_0}{\pi\epsilon_0 h P R_1^2} t\right) \tag{IV.17}$$

The total drift time T can be determined with Equation IV.16 for $r(T) = R_2$

$$T = \frac{\pi\epsilon_0 P h (R_2^2 - R_1^2)}{\mu^+ C U_0} \tag{IV.18}$$

and it can easily be seen that $U(T) = -Nq/C$.

Figure IV.5 (a) shows the time development of the signal for a typical counter tube with $R_2 = 8$ mm, $R_1 = 10$ μm, and an operational voltage of $U_0 = 3$ kV. Figure IV.5 (b) shows calculations for a counter tube with parameters similar to the geometry of a MSPET[4] chamber with $R_1 = 10\mu$m, $R_2 = 1$ mm, and an operational voltage of $U_0 = 1,5$ kV. The mobility for positive charged argon ions is $\mu^+ = 1.7\ \frac{\text{cm}^2}{\text{sV atm}}$ [Sau77]. The capacitance C can be calculated with Equation IV.4. Thus, the total drift time of the ions becomes for (a) $T = 550$ μs and for (b) $T = 10$ μs.

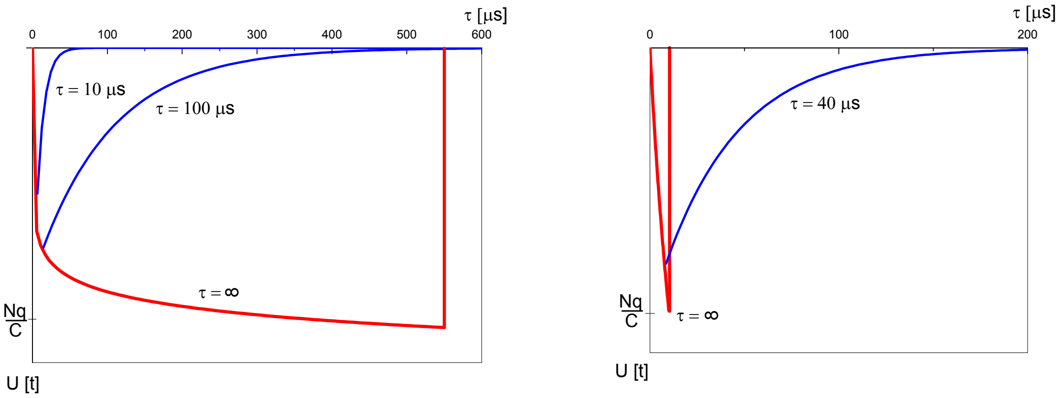

(a) (b)

Figure IV.5: Time development of a signal (a) from a counter tube with a typical geometry and (b) from a counter tube with small dimensions.

---

[4] The *Münster positron emission tomograph* (MSPET) is described in Section V.5.

Due to the long duration of the signal in typical cases, it is normal in practice to terminate the counter with a resistor R, so that the signal is differentiated with a time constant $\tau = RC$. When low impedance resistors are chosen it is possible to measure high fluxes of radiation as the signals become shorter. The differentiation with the RC member let the signal follow the blue lines in Figure IV.5. In Figure IV.5(a) there are displayed two voltage curves for $\tau = 10$ μs and $\tau = 100$ μs. In Figure IV.5 (b) τ was designated to a value around 40 μs to fit to the shape of the signal which has been measured with the MSPET prototype chamber.

Induced Current For further calculations in the next chapter we require the induced current on the wire. The time development of the charge on the wire can be calculated with $Q(t) = CU(t)$ where $U(t)$ is given by Equation IV.17:

$$Q(t) = -\frac{Nq}{\ln\left(\frac{R_2}{R_1}\right)} \ln\left(1 + \frac{t}{t_0}\right) \quad \text{with} \quad t_0 = \frac{\pi\epsilon_0 h P R_1^2}{\mu^+ C U_0} \quad . \tag{IV.19}$$

As the induced current is the derivation of the charge, we get:

$$I(t) = \frac{dQ(t)}{dt} = -\frac{Nq}{2\ln\left(\frac{R_2}{R_1}\right)} \frac{1}{t + t_0} \tag{IV.20}$$

IV.2.6 Region of Limited Proportionality and Geiger-Müller Counter

When the applied voltage of the counter tube is raised, the volume of the region of high electric field intensity grows, thus more gas molecules are ionised. Beyond the region of the proportional counter, the number of slow moving positive charged ions distorts the electric field at the anode which causes the loss of proportionality. This means, that for a single signal this has no influence, but for higher rates this space charge causes a fall of the gas gain which is proportional to the rate [Sau77]

$$M = M_0 \exp^{-(\frac{neT}{4\pi^2\epsilon_0})M_0 R} \tag{IV.21}$$

where R is the flux rate and T is the total drift time of the positive ions. M_0 denotes the gas gain without space charge effects.

If the voltage is raised further, the electrons gain enough energy before they interact with a molecule to produce not only ionised molecules but also excited molecules. The excited molecules cause photons in the UV range which can liberate electrons from the cathode or ionise gas molecules. The produced electrons also cause avalanches with excited molecules which will cause further photons and so on. Thus, the generated pulse becomes independent from the number of primary ionisations. We can see this in Figure IV.3 when the number of collected ions becomes equal for α- and β-radiation whereas α-radiation ionises much more molecules.

When the applied voltage is high enough almost all molecules within the counter tube will be ionised and the liberated charge just depends on the applied voltage U_0 and the capacitance C. A counter tube operating in this region is called a Geiger-Müller counter.

When positive ions are neutralized at the cathode or UV photons hit the cathode electrons can be liberated. These electrons initiate a new avalanche very soon after the primary one, thus a continuous discharge occurs.

To prohibit these continuous discharges two types of self-quenching counters are available. One type uses high resistors, thus the applied voltage falls under the threshold of the Geiger-Müller region when the positive ions drift to the cathode. According to the fact that this mechanism take much time to quench the counter, this counter type cannot operate at high rates.

A second way to quench the counter is to use a polyatomic gas in addition to the filling gas. This gas can absorb the energy of the drifting positive ions or absorb the UV photons. The next section focuses on filling gases and this quenching effect will be discussed in detail. For more details of the mechanisms within the Geiger-Müller region see [Kor46].

IV.3 Filling Gases

Of course the counter tube is not the only type of detector which works on the principle of gas multiplication. Nowadays several gaseous detectors like e.g. the MWPC's, the GEM's or the Micromegas which are used mainly in high energy physics have been introduced.

Gas multiplication depends basically on the migration of electrons rather than on negative ions. Thus, the filling gas for gaseous detectors must be chosen from those types which do not exhibit an appreciable electron attachment coefficient [Kno79]. As air is not one of these, all gaseous detectors must be sealed from ambient air.

The specific experiments have different requirements where low working voltage, high gain operation, good proportionality, high rate capabilities, long lifetime, fast recovery, among others, are examples of sometimes conflicting requirements.

Polyatomic molecules have many non-ionizing energy dissipation modes. Therefore, an inert gas should be the main component of the filling gas if one wants to have a low operational voltage. Xenon and krypton would be the noble gases of choice with high Z which would deliver large cross sections acccording to Equation II.7 or Equation II.17 for photons or energy losses following Equation II.18 for particles. But due to high costs of xenon, argon is used in the most gas detectors as the main component. A pure argon filled counter is not able to deliver gains in excess of $10^3 - 10^4$ without entering into permanent discharge operation. In the avalanche process, excited argon atoms are produced which can only return into the ground state through a radiative process with a minimum photon energy of 11.6 eV [Sau77]. This photon energy is well above the ionisation potential of any metal constituting the cathode (7.7 eV for copper). Thus, the photon can produce a photoelectron at the cathode which can create a discharge in the same way as described in the chapter above.

The large number of non-radiative excited states (rotational or vibrational) of polyatomic molecules can be used to absorb these photons and additionally they also can take up the energy and the charge of the argon ions. The excited molecules dissipate the absorbed energy either by elastic collisions or by dissociation into simpler radicals. The neutralisation of the molecules or radicals at the cathode either produces simpler molecules (dissociation) or forming larger complexes (polymerization). Thus, the probability to liberate electrons is very small.

This quenching property is provided by most organic compounds in the hydrocarbon and alcohol families and also by some inorganic compounds like freons, CO_2, BF_3, and others. Even small amounts of these quenching gases change the operation behaviour of the counter and permit higher gains.

The quenching efficiency grows with the number of atoms in the molecule, so isobutane C_4H_{10} is a good gas to yield high gains, but organic gases have the disadvantage of polymerization. After many ionisations the polymerization process can produce a layer of insulating material on the cathode. The positively charged ions can only leak slowly through the insulator layer. Thus, for high rates of radiation the production rate of ions exceeds the leakage rate. This causes an electric field which can be high enough to extract electrons from the cathode through the insulator into the interior of the gaseous detector where these cause a continuous discharge. Over time the insulator layer thickens, thus the discharge occurs at lower rates. Thereby the lifetime of the detector is shortened.

The highest gains can be reached with electronegative gases like freons.

Additionally to the quenching capability, they can capture free electrons which are liberated at the cathode, but only small amounts should be added to the filling gas because it can also capture electrons from primary ionisations which reduces the efficiency of the detector.

Normally the detectors are connected to an open flow of gas which makes the detectors unhandy as a gas supply system has to be present. A sealed detector would change its operational characteristics after the consumption of all polyatomic molecules or after too much ambient air infiltrates the detector.

CHAPTER V

MWPC and MSPET Prototype Chambers

This chapter uses the basics from the counter tube of the last chapter to derive and to compare the signal developing processes within a MWPC. Thereby the signals differ for the cathode and the anode whereas the signal in a counter tube is equal for the cathode and anode except the sign.

Another topic of this chapter treats the mathematics behind the position reconstruction out of the induced charge on the cathode pads. The second part of the chapter details the mechanical construction of MSPET prototype chambers.

V.1 MWPC

The *multi-wire proportional chamber* (MWPC) is a further development of the proportional counter and was invented 1968 by the group of George Charpak. It was revolutionary for the field of particle detection because the position sensitive MWPC was the first device that was able to determine particle tracks with a electronic readout and it also was capable of measuring much higher rates of particle fluxes than any device before. The MWPC principle is still the main concept for many particle detectors in high energy physics.

The MWPC buildup is a gas filled enclosure which has an anode plane consisting of thin wires and two cathode planes which can be realized either with wires or strips, latter ones are also called *pads*. At one of the cathode planes, the strip direction should be perpendicular to the anode wire direction to be able to determine the position of the avalanche in two dimensions. A scheme of a MWPC is illustrated in

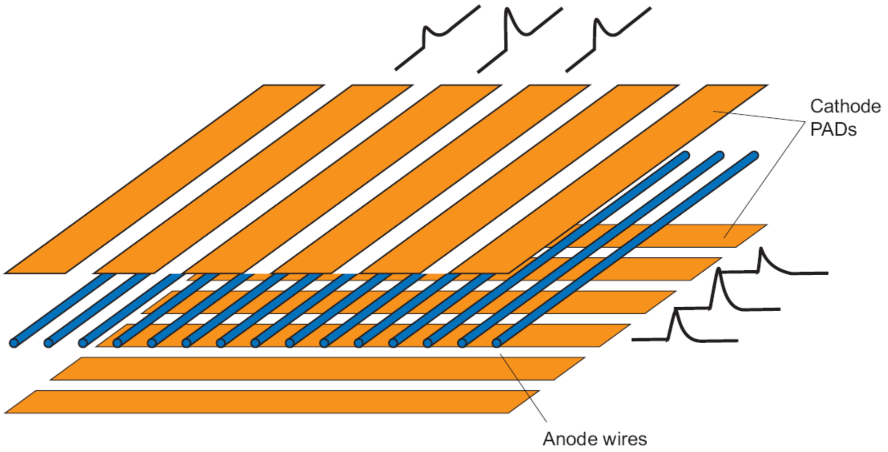

Figure V.1: Schematic setup of a MWPC with pad readout[Pie08].

Figure V.1. Commonly a high voltage is applied to the anode wires and the cathodes are set to earth potential. This makes it easier to determine the position of the avalanche by measuring signals on the cathode strips. It is also possible to determine the position of the avalanche with a read out of the anode wires, but as each anode wire has to be decoupled from the high voltage, and since there are much more anode wires than cathode strips, this should be avoided.

V.2 Signal on the Wires

The electric field of the MWPC can be constructed by linear superposition of weighting fields $\mathbf{E}_n(\mathbf{x})$. The weighting fields are the electric fields where the single electrode n is put on potential V_w and all other electrodes are grounded. For these calculations the both cathode planes can be treated as a single electrode. Therefore, the entire electric field becomes [BRR08]:

$$\mathbf{E}(\mathbf{x}) = \sum_n \frac{V_n}{V_w} \mathbf{E}_n(\mathbf{x}) \tag{V.1}$$

where V_n is the applied voltage at electrode n. The equipotential lines of the electric field within a MWPC are illustrated in Figure V.2.

As the surface charge density is given by $\sigma = \epsilon_0 E$, the total charge on electrode n is given by:

$$Q_n = \epsilon_0 \oint_{\mathbf{A}_n} \mathbf{E}(\mathbf{x}) d\mathbf{A} = \sum_m \frac{\epsilon_0 V_m}{V_w} \oint_{\mathbf{A}_n} \mathbf{E}_m(\mathbf{x}) d\mathbf{A} \tag{V.2}$$

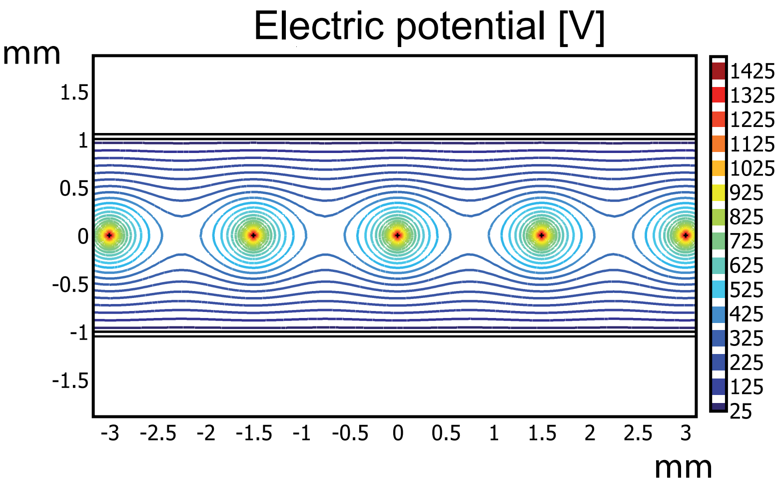

Figure V.2: Equipotential lines of a MWPC with MSPET geometry computed with COMSOL.

where $\mathbf{A}_n$ is the surface of electrode n.
In a system of electrodes the charge on the *n-th* electrode Q_n is related to the applied voltage at the electrodes V_m by the capacitance matrix [Jac75]:

$$Q_n = \sum_m c_{nm} V_m \tag{V.3}$$

By comparing Equation V.2 and Equation V.3 one gets the capacitance matrix elements with

$$c_{nm} = \frac{\epsilon_0}{V_w} \oint_{\mathbf{A}_n} \mathbf{E}_m(\mathbf{x}) d\mathbf{A} \tag{V.4}$$

These capacitance matrix elements c_{nm} are different from the more familiar capacitances C_{nm} that are known from electric circuits. They are related by

$$C_{nn} = \sum_m c_{nm}, \qquad C_{nm} = -c_{nm} \tag{V.5}$$

Setting voltages U_n on the wires results in charges q_n on the electrodes. This is correlated with the capacitance matrix. In Figure V.2 one can see that the electric field is radial close to the wires. As the avalanche occurs near the wire, the electric field is dominated by the charge on the wire and with Equation IV.1[1] the magnitude of the electric field is:

$$E(r) = \frac{q_n}{2\pi\epsilon_0 r} = \frac{1}{2\pi\epsilon_0 r}\left(\sum_m c_{nm} U_m\right) \tag{V.6}$$

---

[1] It is assumed, that the wires are infinitely long, therefore, q_n and c_{nm} are given per unit of wire length so that h drops out in the equation.

By defining the cathodes as electrode $n = 1$ and the wire where the avalanche occurs as electrode $n = 2$ in the approximation for a radial electric field the current on all wires can be calculated with [BRR08]

$$I_w(t) = \sum_n I_n(t) = -\frac{N_{tot} e_0}{4\pi\epsilon_0} \frac{C_{12}}{t + t_0} \quad \text{with} \quad \frac{1}{t_0} = \frac{\mu U C_{12}}{a^2 \pi \epsilon_0} \quad . \tag{V.7}$$

This applies if all wires are set to the voltage U. It is to recognize that this formula is similar to the current induced in the counter tube Equation IV.20.

It is dependent on the amplifiers behind the electrodes if the approximation of a radial electric field is appropriate. For fast amplifiers the ions are within the approximation. For slow amplifiers the approximation is rather worth and the shape of the induced signal is dependent on the angular distribution of the avalanche ions around the wire.

V.3 Signal on the Pads

The signal on one whole cathode plane $I_{c1}(t)$ can be easily obtained if one assumes that the cathode planes are symmetrically arranged to the wires. As the sum of all chamber signals is zero and the signal induced on both cathodes $I_c(t)$ is equal to the negative summed wire signals $-I_w(t)$, the signal on one cathode plane is:

$$I_{c1}(t) = \frac{1}{2} I_c(t) = -\frac{1}{2} I_w(t) = \frac{1}{2} \frac{N_{tot} e_0}{4\pi\epsilon_0} \frac{C_{12}}{t + t_0} \tag{V.8}$$

The whole cathode is subdivided into pads. The weighted field of a pad can be calculated by setting the pad on voltage V_w and all other electrodes on ground as it has been done in Equation V.1. With this method Mathieson gives an exact expression for the weighting field and the induced signal [MF84].

One can calculate a signal on a pad with infinitesimal width and then obtain the whole signal by integrating over the strip width W. This procedure defines a so-called cathode charge distribution $\mathit{\Gamma}(\lambda)$ through

$$dI_{c1}(t) = I_c(t) \mathit{\Gamma}(\lambda) d\lambda \qquad \int_{-\infty}^{\infty} \mathit{\Gamma}(\lambda) d\lambda = \frac{1}{2} \tag{V.9}$$

where $\lambda = x/h$ is the horizontal distance of the infinitesimal strip to the avalanche weighted by the cathode anode gap h.

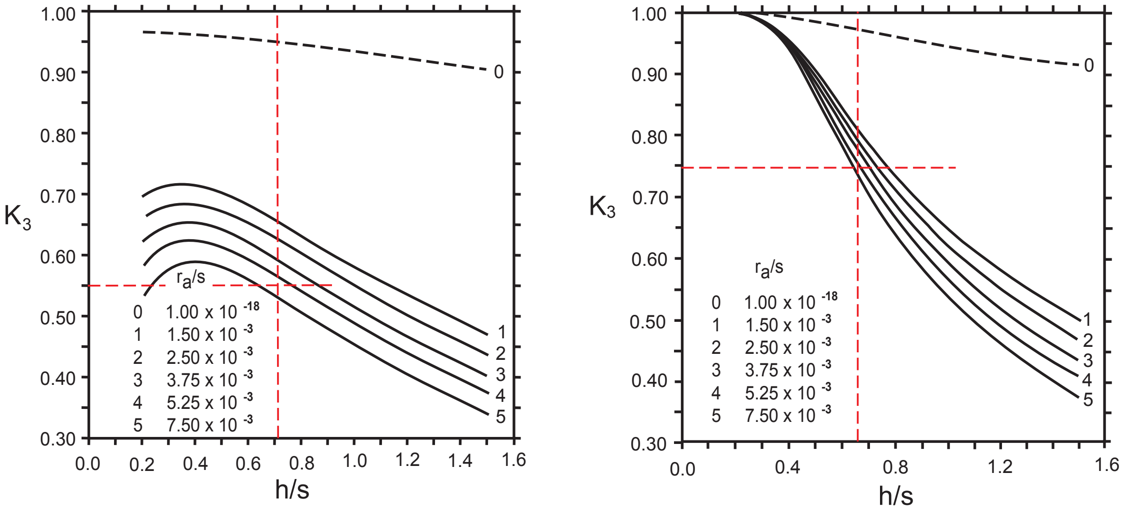

(a) (b)

Figure V.3: The parameter K_3 alters for varying MWPC geometries. Figure (a) shows the K_3 values for cathode pads parallel to anode wire direction and figure (b) the K_3 values for cathode pads normal to anode wire direction [Mat88]. The red lines show the K_3 parameter for the MSPET chamber geometry.

A single-parameter semi-empirical expression for the cathode charge distribution was given by Gatti et al. [GLOS79] and discussed by Mathieson and Gordon [MF84]:

$$\Gamma(\lambda) = K_1 \frac{1 - \tanh^2(K_2\lambda)}{1 + K_3 \tanh^2(K_2\lambda)} \tag{V.10}$$

The parameters K_1 and K_2 are dependent on K_3 with:

$$K_1 = \frac{K_2\sqrt{K_3}}{4\arctan\sqrt{K_3}} \qquad\qquad K_2 = \frac{\pi}{2}\left(1 - \frac{\sqrt{K_3}}{2}\right) \tag{V.11}$$

The parameter K_3 is given for different MWPC geometries in Figure V.3. Here s is the wire pitch and r_a is the wire radius.

The integral of the cathode charge distribution over the pad width W is known as the *pad response function* (PRF) $P_0(\lambda)$ which is proportional to the induced charge on the pad [KB09]:

$$\begin{aligned}\int_{\lambda-\frac{W}{2}}^{\lambda+\frac{W}{2}} \Gamma(\lambda)d\lambda = -\frac{1}{2\arctan\sqrt{K_3}}\Big[&\arctan\left(\sqrt{K_3}\tanh\left(\pi(-2+\sqrt{K_3})\frac{W+2x}{8h}\right)\right)\\ &+\arctan\left(\sqrt{K_3}\tanh\left(\pi(-2+\sqrt{K_3})\frac{W-2x}{8h}\right)\right)\Big]\end{aligned} \tag{V.12}$$

V.4 Avalanche Position Determination

There are several ways to obtain the position of the avalanche within a MWPC, e.g. the wires can be read out at both ends and the arrival time of the signals determine the x-position whereas the wire itself determines the y-position or the centre of gravity of the pad charges can be used to determine the position. In this paragraph only the method which uses a Gaussian fitting curve to estimate the position of the avalanche will be described because it is the method which was used in the experiments of this thesis. The derivation follows the description given by [BR94].

For many chamber geometries the PRF described above can be approximated with a Gaussian curve

$$P_0(x) \approx Ae^{-\frac{x^2}{2\sigma^2}} \quad . \tag{V.13}$$

As the PRF is proportional to the induced charge, one can calculate the charge on three adjacent pads with:

$$\begin{aligned} Q_i &= Be^{-\frac{x^2}{2\sigma^2}} \\ Q_{i+1} &= Be^{-\frac{(x-W)^2}{2\sigma^2}} \\ Q_{i-1} &= Be^{-\frac{(x+W)^2}{2\sigma^2}} \end{aligned} \tag{V.14}$$

The aim is to invert these equations to x. In the first step we derive an equation independent from σ. This is possible with the following charge ratios:

$$\frac{Q_{i+1}}{Q_{i-1}} = e^{\frac{2xW}{\sigma^2}} \tag{V.15}$$

$$\frac{Q_i^2}{Q_{i+1}Q_{i-1}} = e^{\frac{W^2}{\sigma^2}} \tag{V.16}$$

By translating Equation V.16 to $\frac{W^2}{\sigma^2}$ and setting this into Equation V.15, the *displacement* x from the middle of the centre pad to the position of the avalanche becomes:

$$x = \frac{W}{2}\frac{\ln(Q_{i+1}/Q_{i-1})}{\ln(Q_i^2/Q_{i+1}Q_{i-1})} \tag{V.17}$$

This is sufficient to determine the position of the avalanche, but it is possible to improve spatial resolution by determining the displacement with two other charge ratios. These ratios are given from Equation V.14 by

$$\begin{aligned} \frac{Q_i}{Q_{i-1}} &= e^{\frac{2xW+W^2}{2\sigma^2}} \\ \frac{Q_{i+1}}{Q_i} &= e^{\frac{2xW-W^2}{2\sigma^2}} \end{aligned} \tag{V.18}$$

inverting these equations to x gives:

$$\begin{aligned} x &= \frac{\sigma^2}{W} \ln\left(\frac{Q_i}{Q_{i-1}}\right) - \frac{W}{2} \\ x &= \frac{\sigma^2}{W} \ln\left(\frac{Q_{i+1}}{Q_i}\right) + \frac{W}{2} \end{aligned} \tag{V.19}$$

The advancement of this two inverted ratios is that each displacement is calculated just with the charges of two pads. If the avalanche is in the middle of a pad, there will be a signal on three pads, but if the avalanche is between two pads, there will be a signal on just two pads. In those cases where just two pads give a response, Equation V.17 is not a good expression. Therefore, Equation V.17 is used to determine the σ ,which is needed to use Equation V.19, by plotting the displacement against the charge ratio for a given homogeneous data set. Thereafter it is possible to work with Equation V.19 to determine the displacement. The best results are obtained by combining these two equations to a weighted average with the weights w_1 and w_2:

$$x = \frac{1}{w_1 + w_2}\left[w_1\left(\frac{\sigma^2}{W} \ln\left(\frac{Q_i}{Q_{i-1}}\right) - \frac{W}{2}\right) + w_2\left(\frac{\sigma^2}{W} \ln\left(\frac{Q_{i+1}}{Q_i}\right) + \frac{W}{2}\right)\right] \tag{V.20}$$

The square of the charge on the side pads gives a good estimation for these weighting factors $w_1 = Q_{i-1}^2$ and $w_2 = Q_{i+1}^2$. After the displacement has been determined for both cathode planes, it is easy to reconstruct the position of the avalanche within the MWPC.

In the following Equation V.17 will be called *unweighted displacement function* and Equation V.20 will be called *weighted displacement function.*

V.5 MSPET Prototype

V.5.1 Functional Principle

The main concept of *Münster's positron emission tomograph* (MSPET) consists of MWPCs which should detect annihilation photons.

As the probability for ionisation of gas molecules within a MWPC is very low for photons with an energy of $E = 511$ keV, the annihilation photons have to be converted into electrons. For these electrons, which can be produced by the photo electric effect or Compton scattering (Paragraph II.2), the probability to cause gas ionisation is high. To convert a large amount of photons, the converter should be made of a material with high Z, as the cross sections for the photo electric effect and Compton scattering are given by Equation II.7 and Equation II.17.

Measurements from H. Hünteler [Hü07] and simulations from H. Gottschlag [Got10] have shown that the optimal converter thickness is $d = 60\ \mu$m for lead and $d = 35\ \mu$m for gold.

If the converter is thinner, the number of liberated electrons is lower. If in contrary the converter is thicker, the number of liberated electrons drops because there are electrons which stuck in the converter. So the photons which originated these stuck electrons are not detected. When they are detected later in another detector they changed their direction in the first converter and, therefore, they produce scatter coincidences. Hence, the converter thickness should be approximately the optimal converter thickness.

The electrons which are liberated from the converter are not emitted straight forward in the direction of the initial photon. The scatter angles were investigated by H. Hünteler [Hü07] and H. Gottschlag [Got10]. Thus, the electrons are emitted from the converter under a mean exit angle of

$$\alpha_{mean} = 45^\circ \quad . \tag{V.21}$$

The spatial resolution of the MSPET should be better than one millimetre. Therefore, it was decided that the cathode gap has to be one millimetre, so that the deviation from the photon electron conversion to the position of the avalanche is one millimetre in average. Figure V.4 shows a sketch for photon-electron conversion where the electron is emitted under 45°. The electron ionises gas molecules on its track and the electrons from the ionisation are causing avalanches at the wires.

The anode-cathode gap of common MWPCs is about 2-5 mm. So it is not clear

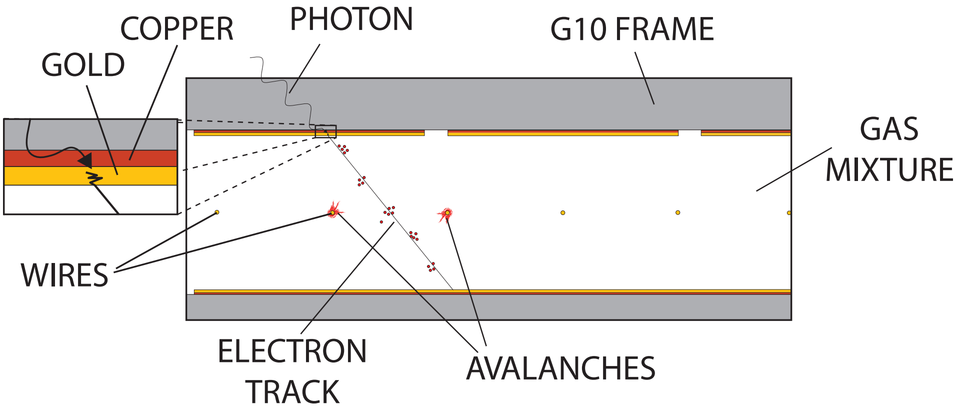

Figure V.4: Sketch for photon-electron conversion with a gold converter within a MWPC with three millimetre pads and a one millimetre anode cathode gap. Inlet shows a zoom of the conservation in the gold layer.

whether a MWPC with such small dimensions is able to provide stable operation. It is also a challenge to manufacture such a MWPC, because the positioning of the wires and the pads have to be very precise.
The production of MSPET prototype chambers has started in 2005 at the *Institute for Nuclear Physic* of the *Westfälische Wilhelms University of Münster*. The first chambers had an anode-cathode gap of three millimetre and a pad width of 9.7 mm and different designs to implement the converter have been investigated. For a elaborate description of the evolution of the prototypes the reader is referred to [Got10].

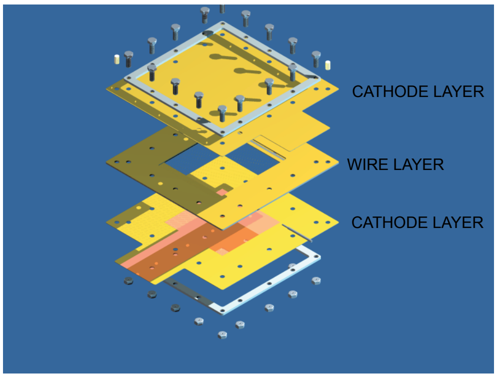

Figure V.5: Engineering drawing of a MSPET prototype chamber.

V.5.2 Details for the Construction of a MSPET Chamber

This section provides some details on the detector geometry and information about the construction steps for the latest MSPET prototype chamber.

All MSPET prototype chambers, which were produced, have a wire pitch of $s = 1.5$ mm. The pad width of the newest chambers is 3 mm. The frame of the chamber is made of FR4. This is a compound of woven glass and epoxy which is usually used for printed circuit boards. It is a good insulator, does not outgas, and the mechanical stability is good.

Two layers which were covered with copper on one side were used. These are commercially available and can be used to produce the two cathode layers. A photo etching process, which is normally used to create the tracks on the circuit boards, can be applied to remove the copper which is not necessary for the cathode pad geometry. The whole layer has an area of 20×20 cm^2 and the copper cathodes cover an area of 10×10 cm^2.

The wires with a diameter of $d = 20$ μm were arranged first on a large aluminium frame. Therefore, a hand driven machine was used to hold the wires on a constant pitch and gave them a defined tension of 0.5 N. Later the wires were glued on a FR4 frame which is one millimetre thick and has the same size as the layer for the cathode planes. A second frame with similar geometry was then glued on the first one, so that the anode-cathode gap becomes one millimetre on both sides. These two layers from here on are called the wire layer. Hence, the chamber provides a volume for the gas mixture of $V = 10 \times 10 \times 0.2$ cm^3. Figure V.5 shows a drawing where the different layers combined with an aluminium frame and some screws build the whole chamber. The converter can be realized as a gold layer on the cathode pads.

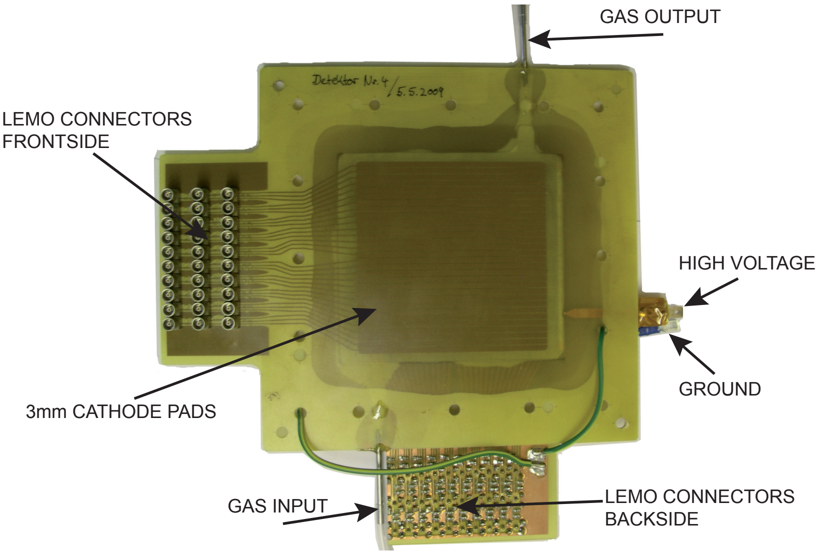

Figure V.6: Photograph of a glued MSPET prototype chamber with three millimetre pads.

One chamber with a gold converter was produced up to now. The gold layer was electroplated by the company *Drollinger*.

The two cathode layers can either be glued or screwed to the wire layer. The glued version has the advantage that the electrodes are arranged very precise in altitude and that the chamber is very airtight. The disadvantage is that the chamber cannot be opened again if something went wrong. For screwed chambers gaskets are needed and it is much more difficult to reach the same precision in electrode positioning and airtightness. A photograph of a one millimetre prototype chamber is illustrated in Figure V.6.

CHAPTER VI

Efficiency to detect Conversion Electrons

Efficiency calculations of a MSPET scanner with 200 detectors were shown by H. Hünteler [Hü07]. He implemented the suggestion, that every electron that is liberated from the converter has to produce a measureable avalanche. Therefore, the efficiency to detect charged particles of a prototype chamber has to be determined. This chapter presents efficiency measurements performed with cosmic radiation.

VI.1 Measurement Principle

Cosmic radiation consists mainly of protons and α-particles which cause so called *air showers* by interacting with molecules when they enter the atmosphere. As a result there is a continuous flow of muons $I \approx 1\ \mathrm{cm}^{-2}\mathrm{min}^{-1}$ at sea level with an mean energy of $E \approx 4$ GeV [A$^+$08]. The number of different charged hadrons and leptons which are created in the air showers is dependent on the altitude. This is depicted in Figure VI.1 for particles with $E > 1$ GeV.

At sea level there are also electrons and positrons of lower energies. The dominant source of them is the muon decay. The integral vertical intensity of electrons plus positrons is very approximately 30, 6, and 0.2 $\mathrm{m}^{-2}\mathrm{s}^{-1}\mathrm{str}^{-1}$ above 10, 100, and 1000 MeV respectively [A$^+$08].

Minimum ionizing particles produce 94 ion pairs per cm in argon [Sau77], so that there are produced at least 18.8 electrons within the two millimetre thick MSPET chamber when an ionised particle crosses the gas layer perpendicular. The minimal energy loss in argon is for electrons with energies around 1 MeV [BCZC05].

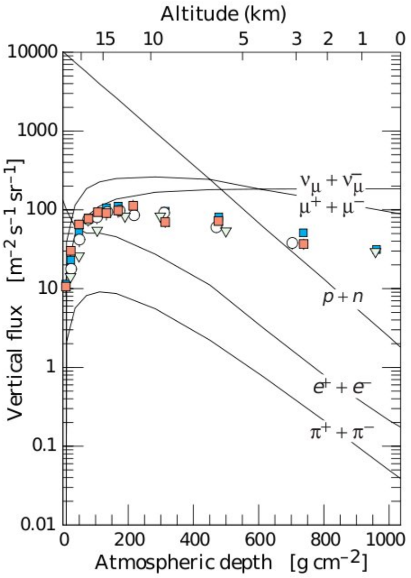

Figure VI.1: Vertical fluxes of cosmic rays in the atmosphere with $E > 1$ GeV estimated from the nucleon flux. The coloured data points show measurements of negative muons [A^{+}08].

Therefore, the MSPET chamber should be capable of detecting all high energy muons or electrons which cross the detector.

To determine when a cosmic muon or electron crosses the detector, two scintillation detectors has been constructed and the MSPET chamber was positioned between them, what can be seen in Figure VI.2.

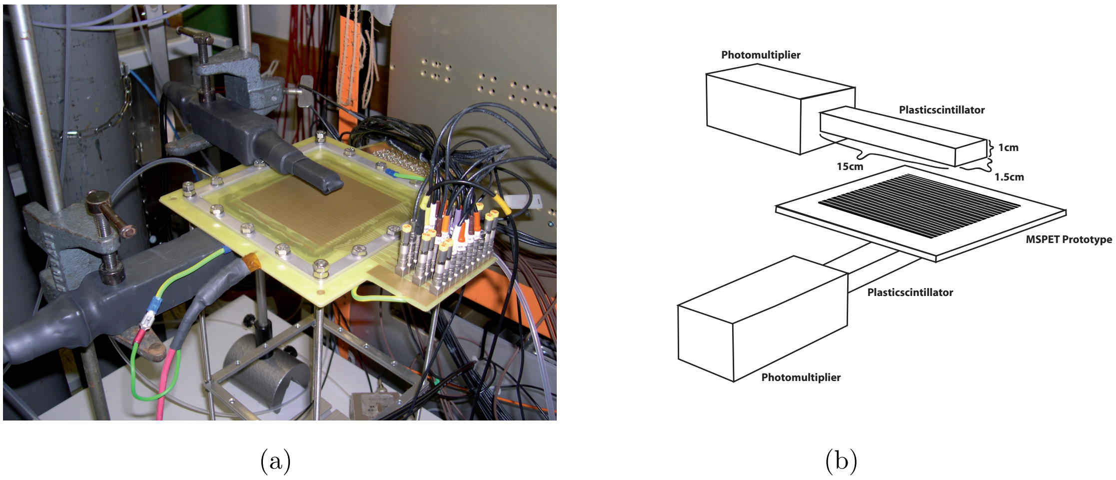

(a) (b)

Figure VI.2: Detector alignment for efficiency measurements with cosmic rays.

The scintillation detectors were constructed with a $15 \times 1.5 \times 1$ cm^3 large plastic scintillator coupled to a VALVO XP2972/PB photomultiplier tube. They were shielded from ambient light with insulating tape and heat shrinkable sleeves.

Gas Flux Regulation A gas flux regulation system has been installed to produce different gas flow ratios. The system consisted of the *multi gas controller* (mks MGC 647C) which is able to control four *mass-flo controllers* (MFC). In the measurement setup the MGC was connected to three MFCs Type 1179B which were also from mks. Each MFC handled one gas component.
One MFC has been specially calibrated with argon for a maximal gas flow of ten liters per hour. This equates to $166.\overline{6}$ sccm [1]. The two other MFCs have been calibrated with nitrogen for a maximal gas flow of 50 sccm.
One of these MFCs operated with carbon dioxide and the other with isobutane. The gaskets of the MFC which operated with isobutane were made of kalrez which is a Perfluorelastomer since normal gaskets would be destructed by the gas.
The MGC needs a *gas correction factor* (GCF) and the maximal gas flow of each MFC for the calibration gas to adapt the applied gas to the calibration gas of the MFC. The GCF for carbon dioxide is 0.7 and for isobutane 0.27.
With these GCFs the maximal gas flow for carbon dioxide becomes 35 sccm and for isobutane 13.5 sccm. The minimal gas flow is 1 % of the maximal gas flow.
From the calibrations made by mks the error of the gas flow of nitrogen (argon) is $< 0.2\%$ of the maximal gas flow.

A problem with the MFC for argon was given. For the operation with argon the GCF would be one as the MFC has been calibrated with argon. The problem was that the maximal gas flow could only be set to 150 sccm or 200 sccm at the MGC but the MFC had a maximal gas flow of $166.\overline{6}$ sccm. To overcome this problem the maximal gas flow was set to 200 sccm and the GCF was set to 1.2. Consequently one had to set a flow which is 1.2 times larger than the desired flow.

---

[1] sccm = standard cubic centimetre per minute
A measurement of airflow that indicates how many cubic centimetre of air pass by a stationary point in one minute under standard conditions of temperature, pressure, and humidity. In this case the standard pressure is 1013 mbar and the standard temperature is 0°C (DIN 1871).

VI.2 Details on Signal and Data Processing

The whole measurement setup with detailed view on signal processing is depicted in Figure VI.3. A sophisticated *Labview*[2] program has been designed which was primary built to count the coincidences from the two scintillators and the coincidences from all three detectors. The ratio of these two values gave the efficiency of the chamber to detect high energy muons and electrons from the cosmic radiation and thus the efficiency to detect small amounts of electrons within the gas volume. In order to the small interaction area for triple coincidences which was 2.25 cm^2 (scintillation detectors were arranged perpendicular), the rate of coincidences was very low. Therefore, much time was needed to get enough statistics for the evaluation.

VI.2.1 Problems in Data Acquisition

A significant problem with long time measurements has been that a continuous discharge could occur at any time of the measurement when the applied voltage was too high. To prevent the detector from damage, the high voltage droped down if the current exceeds 100 μA.

The *Labview* program monitored the high voltage. When the high voltage breaked down it was reseted. Therefore, it was possible to measure over several days.

Nevertheless, long dead times up to one or two minutes were unavoidable due to the serial connection from the computer to the high voltage module. The serial connection did not provide a continuous monitoring of the high voltage. Therefore, the *Labview* program needed some time to give a response on a voltage drop. The voltage ramp which followed this response also took some time.

Another big problem was that electronic disturbances arised in the electronic setup when the voltage was ramped down abrupt which caused additional signals on the counters.

For moderate gains the probability for continuous discharge was low. Hence, the current exceeded the 100 μA threshold for voltage drop down just one or two times a day, but with increasing gain the number of discharges which disturb the measurement went up as well.

---

[2] **Lab**oratory **V**irtual **I**nstrumentation **E**ngineering **W**orkbench is a visual programming language from National Instruments for the development of control programs.

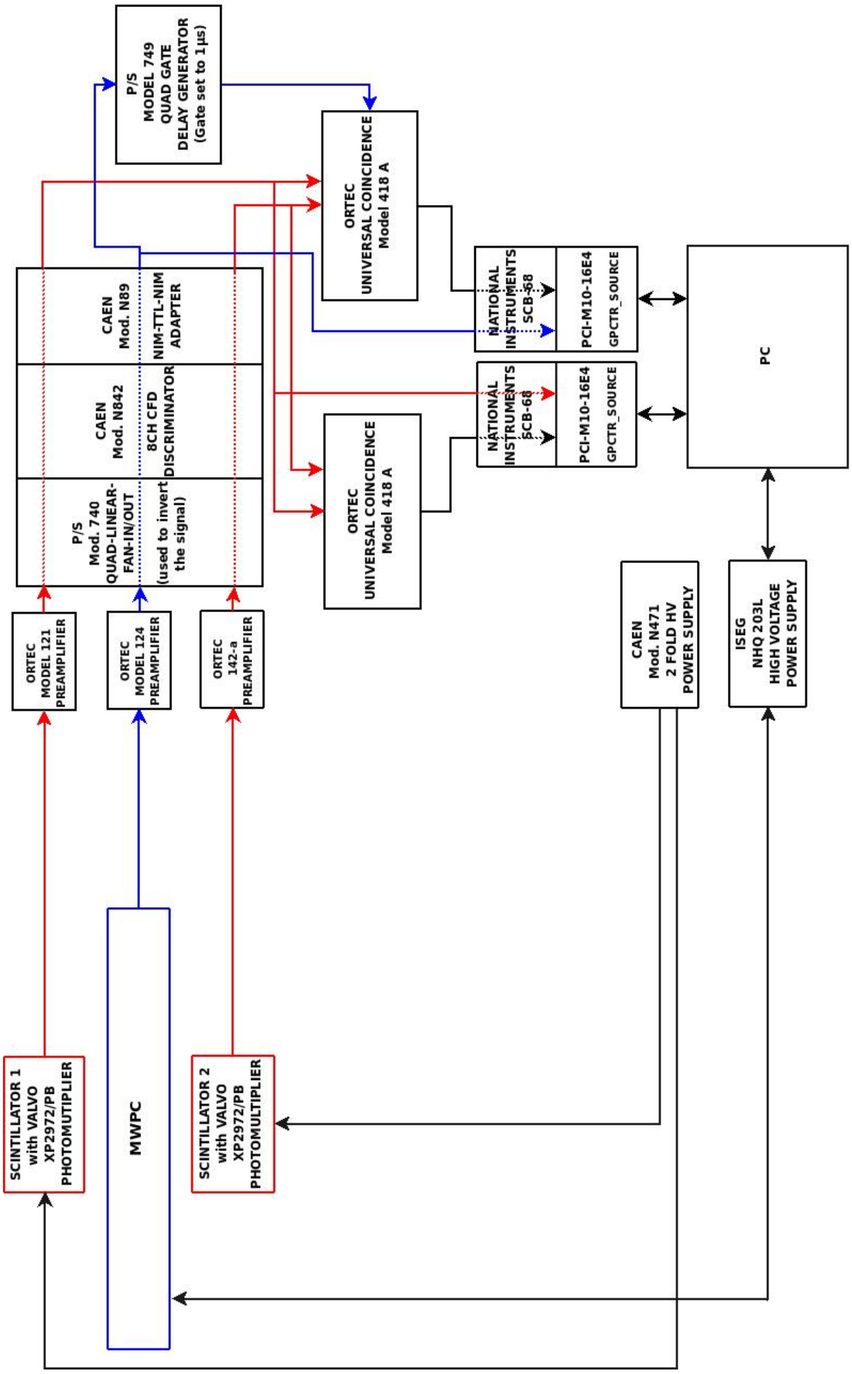

Figure VI.3: Layout of the electronic components of the measurement setup.

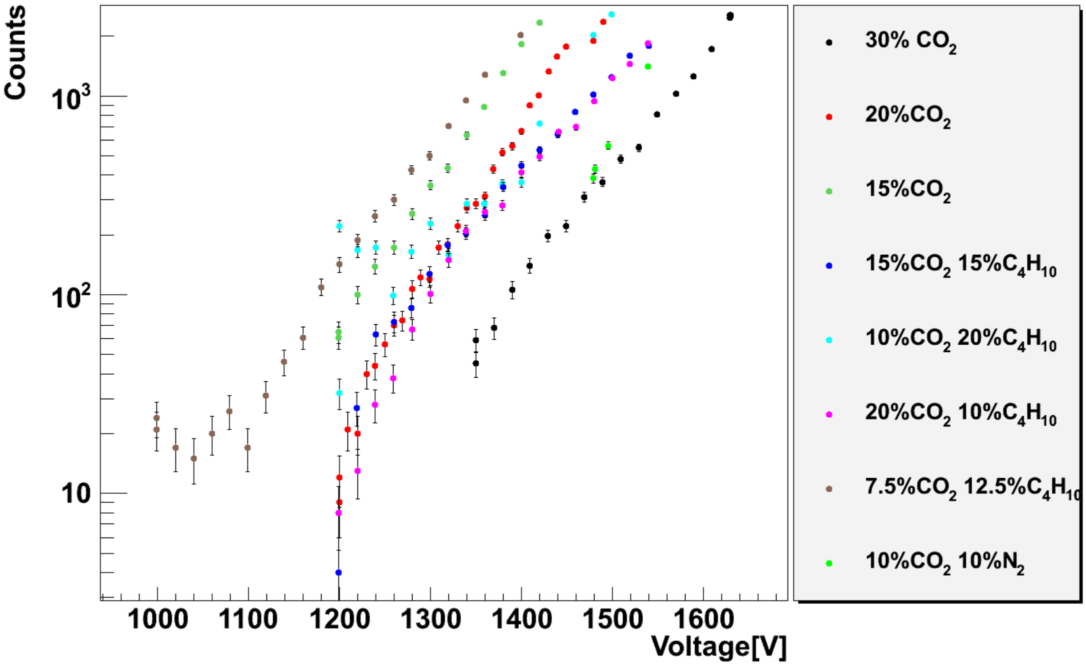

Figure VI.4: Count rate performance of the MSPET Prototype for different gas mixtures. The main component of the gas mixture was argon.

VI.2.2 Additional Features

The Labview program counted the signals produced from one scintillator and from the MSPET chamber. It counted also how many voltage breakdowns had occured. This data could be used to check if the counters had worked stable during the measurement, just by looking if they had reasonable values.

The ability to determine the count rate of the MSPET chamber was used before each efficiency measurement. The results are presented in Figure VI.4. Each data point here represents a 15 min. measurement of cosmic radiation. Assuming that there was a cosmic muon flux of $I \approx 1$ cm^{-2}min^{-1}, the count rate should not exceed a value of 1500. Of course, there is also a electron component in cosmic radiation, but it is not clear which electrons in the energy range of 1-1000 MeV are able to pass all three detectors. Nevertheless, the electron fraction at sea level is just about 20% [Gru06]. Thus, we see that the MSPET chamber detected more signals than could be produced by cosmic radiation at high gains. It seems that secondary avalanches were produced and detected at higher gains.

Furthermore, we could not find a plateau where a continuous flux of radiation was measured.

VI.3 Results

The efficiency measurements have been performed with eight different gas mixtures. Each data point in Figure VI.5 represents five hours of measurement time. The main component of all gas mixtures was argon and a gas flow of 20 sccm was used. In the first three measurements the fraction of the quenching gas CO_2 was variated between 15% to 30%.

The performance with a fraction of 30% quenching gas was the most stable one which means that less voltage breakdowns were observed for medium gains and it was also possible to perform measurements with a high fraction of voltage breakdowns.

In following measurements a varying fraction of isobutane C_4H_{10} within 30% fraction of quenching gas was given. Isobutane has a better quenching ability due to more atoms within a molecule.

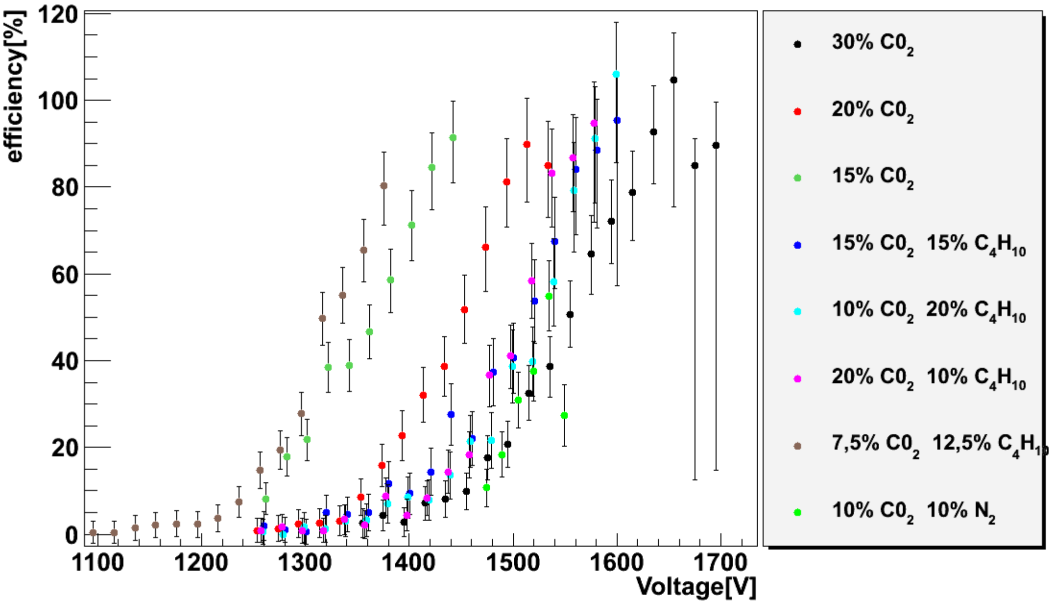

Figure VI.5: Efficiency of the MSPET Prototype to detect cosmic muons or electrons for different gas mixtures. The main gas component was argon. Each data point represents a measurement of five hours. Error corrections due to high voltage breakdowns were made.

In Figure VI.5 one can see that all mixtures with 30% quenching gas reach a value between 90% and 100%. Due to the errors one cannot determine that any composition would deliver a higher efficiency, but one can clearly see that there is a tendency of weaker performance for lower fractions of quenching gas.

The composition with 30% CO_2 was the only one which was able to work at higher voltages after reaching the region with efficiencies around 100%.

Therefore, it was decided to use this gas mixture for all upcoming measurements.

VI.3.1 Errors

For the absolute errors in Figure VI.4 and Figure VI.5 the square root of the number of counts was used following counting statistics. In the calculations of the efficiency error there was an additional systematic and lower error. The systematic error was determined with a measurement where the scintillation detectors were placed separately from the MSPET prototype. The response of the system gaves an efficiency of 2.22%, although no coincidence could occur in reality.

The lower error arises from the problems discussed in Paragraph VI.2.1. In detail, this denotes that the counter counted up coincidences when a discharge occured although no cosmic muon or electron hits the detectors. In this cases it could happen that the coincidence counter for the scintillation detectors counted up just one while the counter for triple coincidences counted up two. Due to this strange behaviour it was possible that we obtain efficiencies over 100%. Because of this misbehaviour the relative lower error was calculated with the number of high voltage breakdowns N_{VB}, the number of coincidences of the scintillators N_2, and the number of triple coincidences N_3

$$\sigma_{low} = \sqrt{\sigma_{sys}^2 + \sigma_{N_2}^2 + \sigma_{N_3}^2 + (\frac{2N_{VB}}{N_2})^2}$$

where σ_{sys} is the systematic error and σ_{N_2}, σ_{N_3} are the relative errors of the coincidence measurements.

VI.3.2 Additional Measurements

Efficiency measurements with 20 sccm and 30 sccm gas flow were made. The gas flow assigns the pressure inside the chamber.

Five measurements with a measurement time of 15 hours and a 80/20 mixture of Ar/CO_2 gas were done for the 20 sccm gas flow setting. The high voltage was set to

1700 V. These measurements are compared to three measurements with a gas flow of 30 sccm which were performed under the same conditions.
The mean values are

$$\begin{aligned} 20\ \text{sccm}: \quad & \frac{N_3}{N_2} = (24.43 \pm 4.13)\% \\ 30\ \text{sccm}: \quad & \frac{N_3}{N_2} = (19.06 \pm 3.84)\% \end{aligned}$$

The error is the product of the systematic error and the standard deviation.
This indicates that a higher gas flow would not improve the efficiency of the detector. But the big error makes it difficult to determine an optimal gas flow. Further measurements are necessary to determine the optimal parameters for the chamber.

CHAPTER VII

Spatial Resolution

The inherent spatial resolution of a MSPET prototype chamber is important to estimate the spatial resolution of the whole MSPET. As it is not trivial to produce a collimated beam of 511 keV photons, a X-ray source was used to determine the spatial resolution of the chamber. The first part of this chapter describes the energy spectrum of the X-ray source and shows the theoretical transmission for the MSPET chamber. Then the electronics and the instruments of the measurement setup are described. After the general detector response on uncollimated X-rays is presented, measurements to determine the spatial resolution are shown. Finally the last section illustrates some experiments which were not able to determine the spatial resolution.

VII.1 X-ray Source and Transmission

An energy spectrum of the X-ray source was measured by C. Baumann [Bau09]. The X-ray source and the energy spectrum are shown in Figure VII.1. One can see that the X-ray source produces a continuous spectrum between 6 and 10 keV.

It is not possible to inject the X-rays directly into the gas layer of the chamber as the gas layer is sealed from ambient air by its frame. Therefore, the X-rays have to pass the 0.5 mm thick FR4 frame and the 35 μm copper layer of the cathode pads before they can ionise molecules in the gas layer. The number of photons that reach the gas layer is dependent on the mass attenuation coefficient of the material. The transmission can be calculated with Equation II.4. The density of copper is $\rho = 8.92\ \frac{\mathrm{g}}{\mathrm{cm}^3}$. For simplicity one can approximate that the FR4 frame consists of

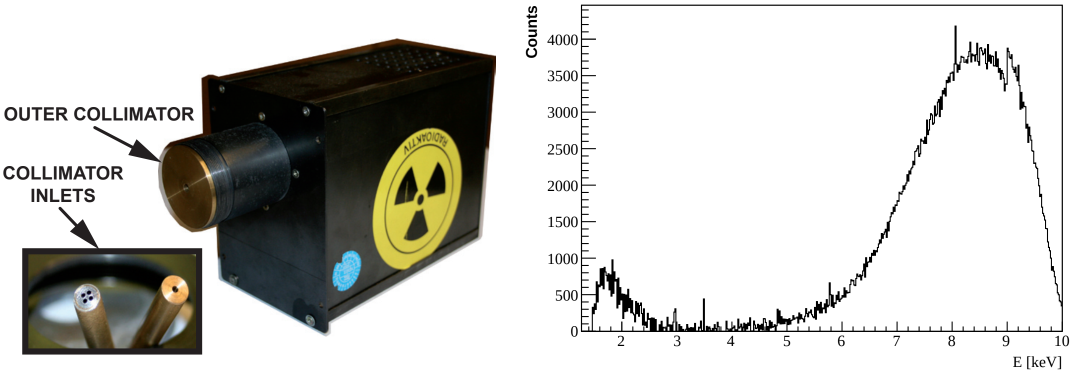

(a) (b)

Figure VII.1: (a) Photograph of the X-ray source with a zoom on two collimator inlets. (b) Energy spectrum of the X-ray source.

carbon[1] and has a density of $\rho \approx 1.7\ \frac{\text{g}}{\text{cm}^3}$. The main component of the gas mixture is argon and the density of gas under atmosphere pressure is $\rho = 0.001784\ \frac{\text{g}}{\text{cm}^3}$.
A parametrization of the total photon *mass attenuation coefficient* (MAC) has been investigated by Orlic et al. [OLS+93]. They found the semi-empirical formula:

$$\frac{\mu}{\rho} = exp\big(p_1 + p_2(\ln\lambda) + p_3(\ln\lambda)^2 + p_4(\ln\lambda)^3\big) + \sigma_c^e Z N_A/A \tag{VII.1}$$

with $\lambda = 12.3981/E(\text{keV})$. σ_c^e is the Compton cross section for an electron given by Equation II.16. The parameters p_1, p_2, p_3, and p_4 are a set of fitting coefficients. Each set is valid between two absorption edges and tabulated for all energies between 0.1 - 1000 keV in [OLS+93]. With these MACs the transmission was calculated for the parameters described above and are shown in Figure VII.2(a).
The jumps in the transmission curves for the copper and gas layer come from the absorption edges of the materials. The absorption edge for the K-shell for copper is at an energy of $E_K = 8.9789$ keV and the absorption edge for the K-shell for argon is at an energy of $E_K = 3.2029$ keV. A cross check was performed by calculating the transmission also with XCOM[2] data which is available at [BCZC05].

---

[1] Even if the FR4 consists mainly of carbon, the transmission is properly lower as the heavier elements in the FR4 cause a much higher attenuation. However, for the experimental evaluation a rough estimation of the transmission is sufficient as the FR4 layer is steady distributed over the whole detection volume.

[2] As the semi-empirical formula from Orlic et al. was derived from XCOM data, it has to provide the same transmission.

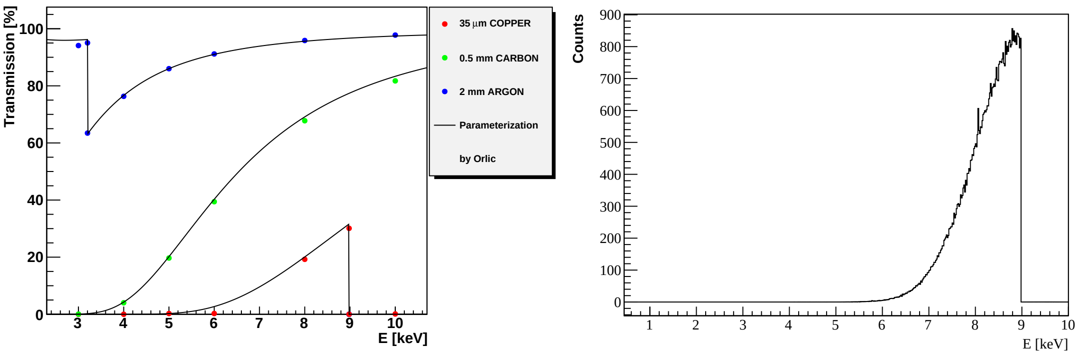

(a) (b)

Figure VII.2: (a) Transmission curves for different photon energies. The jump of transmission in the copper layer comes from the K absorption edge. The points represent calculations with XCOM data. (b) Spectra of the X-ray source used in the experiment convolved with the transmission curves for copper and carbon layers.

These calculations are depicted by the coloured points in Figure VII.2(a). The energy spectrum of the X-ray source convolved with the transmission curves for the copper and carbon layers are shown in Figure VII.2(b).

VII.2 Measurement Setup

To perform the spatial resolution measurements a setup was designed where the X-ray source was screwed to a fixed position. To be able to irradiate different positions on the MSPET prototype chamber a carrier for the chamber was mounted directly in front of the X-ray source. The carrier could be moved in horizontal and vertical direction with a precision of $\sigma_{x,y} \approx 100$ μm which was given by the accuracy in turning the rotating head of the all-thread rod. In Figure VII.4 a technical drawing and a photograph of the measurement setup are illustrated.

The X-ray source could be equipped with different collimators, which were made of brass, to produce different beam shapes. Measurements were made with collimators which had an inner diameter of one millimetre, 200 μm, 100 μm or 50 μm. Additionally a collimator with four pin-holes where the centre of the holes had a distance of one millimetre each and each pin-hole had a diameter of 750 μm was produced. The collimators with an inner diameter under 200 μm and the four pin-hole collimator were made of a collimator with an inner radius of three millimetres.

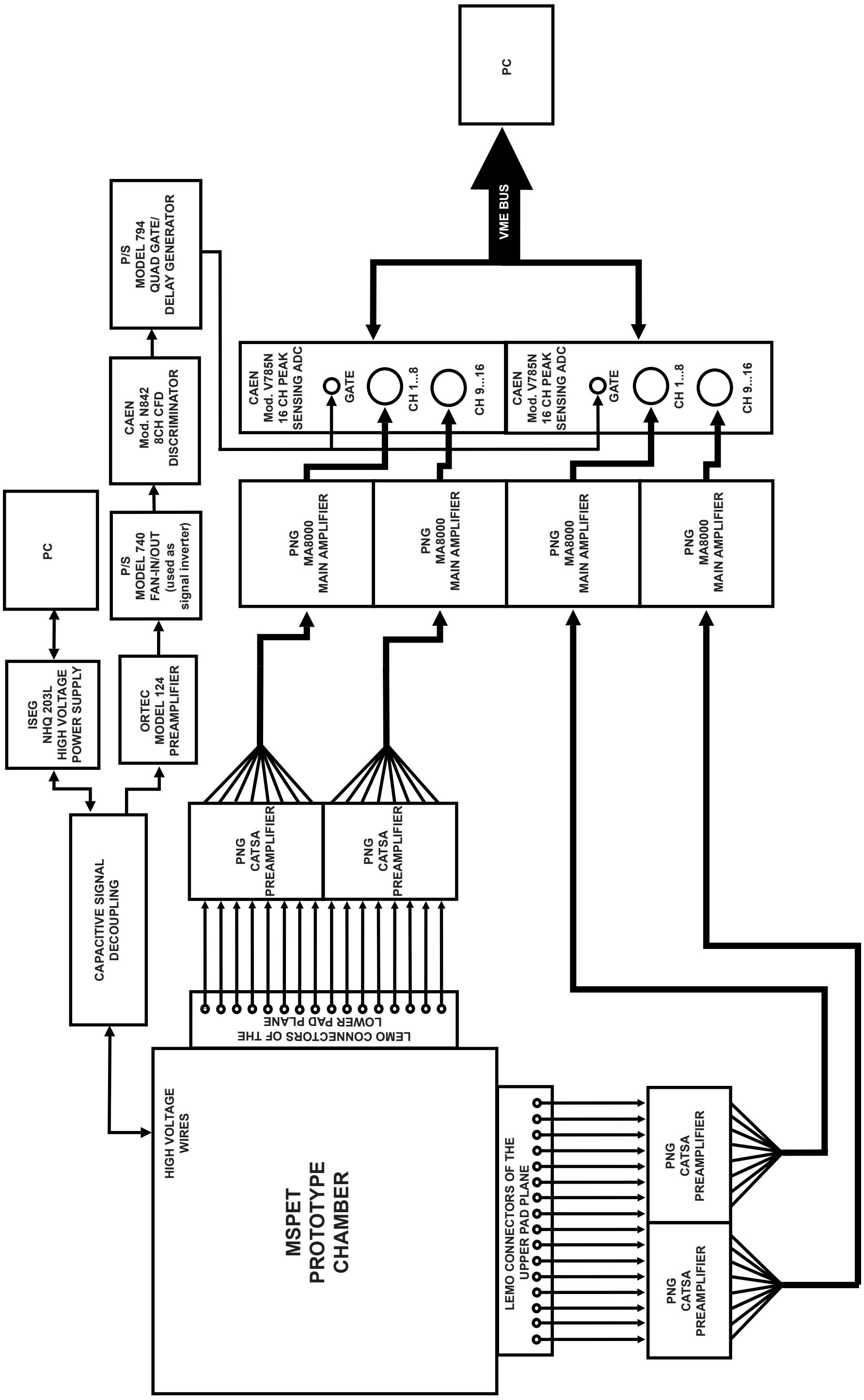

Figure VII.3: Layout of the electronic components of the setup for the spatial resolution measurements.

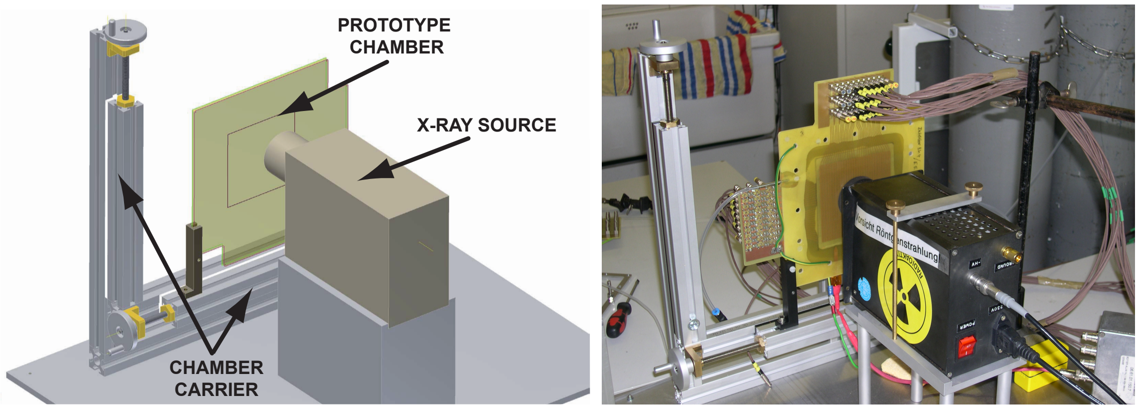

(a) (b)

Figure VII.4: (a) Technical Drawing of the measurement setup. (b) Photograph of the measurement setup with a MSPET prototype chamber.

The inner hole was filled with a one millimetre thick layer of solder and the pin-holes were drilled into this layer. A zoom on two of these collimator inlets is presented in Figure VII.1(a). The source was also used without a collimator to irradiate the whole detection area of the chamber.

The signals on the pads of the chamber were amplified by a pre-amplifier (PNG CATSA) and shaped by a main amplifier (PNG MA8000). The signals were then digitized by a peak sensing ADC (CAEN Mod.V785N) and processed with a PC. As the ADC needed a gate in which it determined the maximum signal height, the signal on the wires was decoupled from the high voltage and processed electronically to provide a 10 μs long gate. The entire electronic setup is illustrated in Figure VII.3.

VII.3 Chamber homogeneously irradiated with X-Rays

The reconstruction of the position of the avalanche out of the measured data with the weighted displacement function requires the determination of a PRF-σ as described in Section V.4. To determine an appropriate PRF-σ the chamber was irradiated by the X-ray source without a collimator.

The gas inside the chamber was not irradiated homogeneously as there is a gap between the adjacent cathode pads of 0.3 mm. The transmission curves for the different materials shown in Figure VII.2(a) indicate that the amount of radiation that passed the FR4 layer between two pads was much larger than the amount of radiation which passed the FR4 and the copper layer. This produces a symmetrical pattern of reconstructed avalanche positions when the chamber was irradiated homogeneously.

A homogeneous irradiated MWPC shows also an inherent pattern as every avalanche occurs very close to a wire. Therefore, the pattern of reconstructed avalanche positions of the MSPET prototype chamber is a combination of a transmission pattern and a wire pattern.

A way to determine the PRF-σ was described in Section V.4. The reconstructed hit maps showed only a rough image of the expected pattern when the PRF-σ was dirived with this method.

As the theoretical patterns are known, a more appropriate PRF-σ could be determined by varying the PRF-σ until the reconstructed pattern fit to the expected pattern.

This method was applied and the results are displayed in Figure VII.5. As the transmission pattern is varying just in one dimension, this pattern can be rejected by projecting the 2D hit map into the other direction.

The cathode pads which cause the transmission pattern were arranged perpendicular in the both layers. Therefore, it was possible to reject the transmission pattern in both directions by simply turning the chamber through 180°. Figure VII.5(a),(b) show the 2D hit maps where the transmission and the wire pattern are overlapped. Figure VII.5(c) shows the projection of (a) to the y-axis. As the transmission pattern is rejected and the wire pattern varies just in the x-direction, the histogram should show a continuous distribution. The peaks are reconstruction artefacts which occur as the ratio from pad width to anode-cathode gap reaches a limit for reasonable reconstruction via charge separation[3]. The PRF-σ was optimised in such a way that the peaks were as low and as thin as possible and the best achievable result that is shown in the figure was reconstructed with PRF-$\sigma_y = 0.119$ cm.

Figure VII.5(d) shows the projection of (b) to the x-axis. As the transmission pattern is rejected, only the wire pattern can be seen. The distance between the unique peaks should be 1.5 mm which is the wire pitch. The PRF-σ was optimised in such a manner that the peak distance was as close to the expected value as possible and the best achievable result that is shown in the figure was reconstructed with PRF-$\sigma_x = 0.128$ cm.

---

[3] Details are treated in chapter VIII.3.

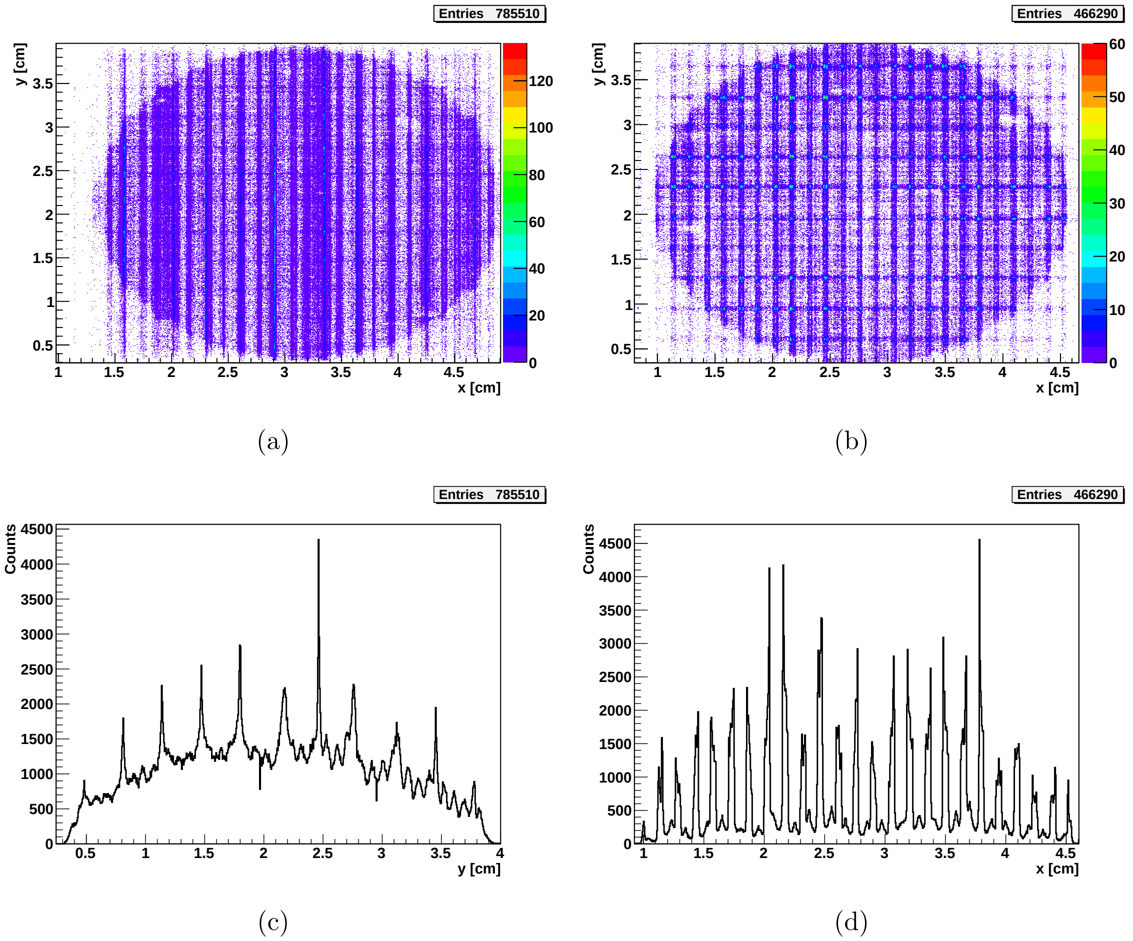

(a)

(b)

(c)

(d)

Figure VII.5: (a) 2D hit map. The chamber was irradiated with the uncollimated X-ray source. The wires were orientated in the y-direction. The radiation had to pass the cathode layer which was parallel to the wires. (b) 2D hit map. The chamber was reversed. Hence, the radiation passed the cathode layer which was perpendicular to the wires. (c) Projection from (a) to the y-axis. The peaks are reconstruction artefacts. (d) Projection from (b) to the x-axis. The peaks were produced by the wires.

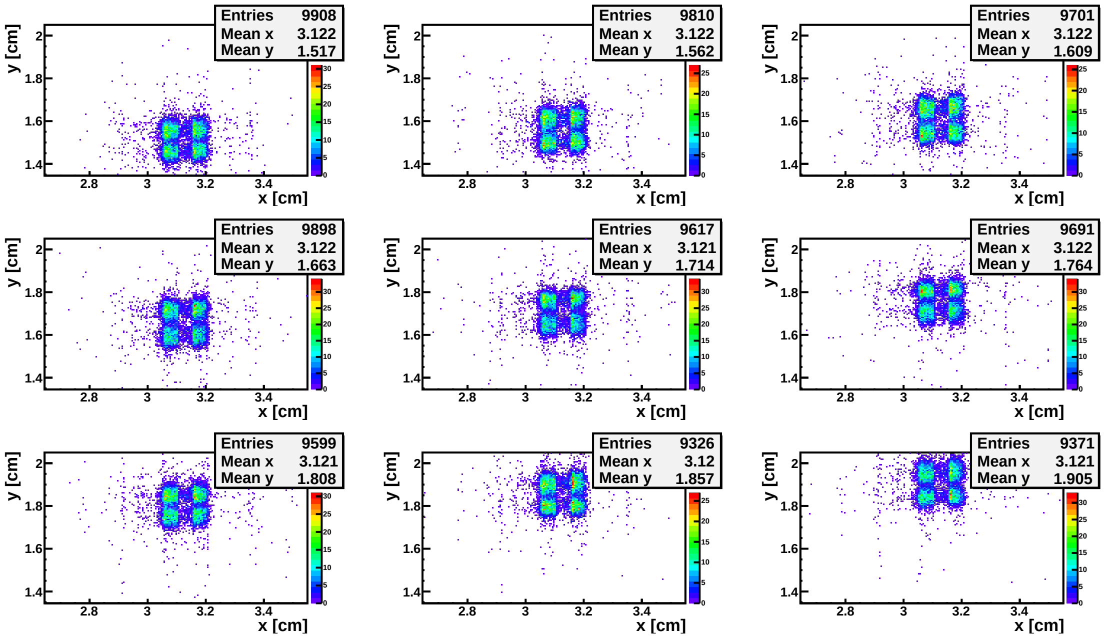

Figure VII.6: 2D hit maps. The chamber was irradiated with the X-ray source which was collimated with the four pin-hole collimator. The chamber was moved in y-direction in 500 μm steps.

VII.4 Measurements with the Four Pin-Hole Collimator

Thirty single measurements with the four pin-hole collimator were performed for each direction. In each measurement the source irradiated the chamber five minutes long and was then moved 500 μm forward in one direction. It was assured that the X-ray source was moved along a pad, so that the transmission pattern had no influence on the measurement. The 2D hit maps of the first nine measurements of each direction are shown in Figure VII.6 and Figure VII.7. They illustrate that the beam shape caused by the four pin-hole collimator stayed constant when the source was moved in the y-direction and was strongly influenced by the wires if the source was moved in the x-direction. The images show that the single beams could be separated, which indicates, that the spatial resolution is below one millimetre as the pin-holes had a deviation of one millimetre.

A Gaussian fit was applied on each peak and the deviation of the mean values of the fits defined the distance of the peaks. As the centre of the pin-holes of the collimator had a distance of one millimetre, the deviation of the reconstructed peak distance

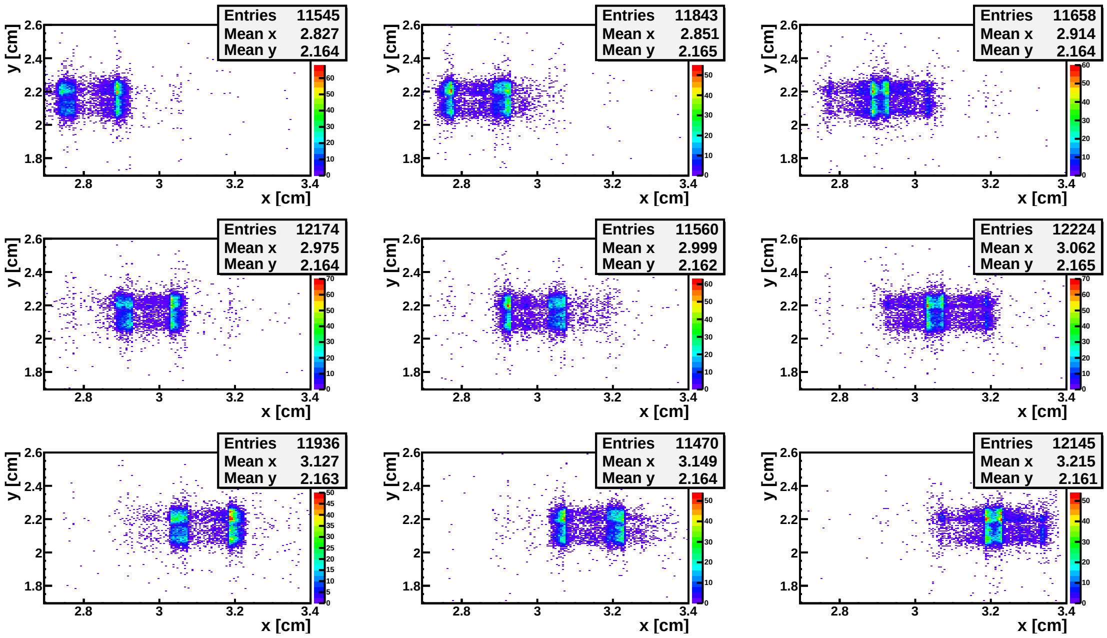

Figure VII.7: 2D hit maps. The chamber was irradiated with the X-ray source which was collimated with the four pin-hole collimator. The chamber was moved in x-direction in 500 μm steps.

to one millimetre gave more information about the obtainable spatial resolution of the chamber. Figure VII.8 shows the deviations from the millimetre for all sixty measurements. The mean value ρ of the deviations from one millimetre is

$$\rho_x = 432\ \mu\text{m} \pm 171\ \mu\text{m} \qquad \text{and} \qquad \rho_y = 138\ \mu\text{m} \pm 75\ \mu\text{m} \tag{VII.2}$$

where the uncertainties are given by the standard deviation.

The position in x-direction is restricted to the position of the wire. Therefore, the position of the incident radiation can only be determined with an accuracy of half the wire pitch s to both sides of the wire. It is just known that the incident radiation was within this interval. The probability of the position is, therefore, given by an uniform distribution. The probability density function is then $f(x) = 1/s$ within the interval and zero outside the interval. The variance of such a distribution is given by:

$$Var(x) = \langle x^2 \rangle - \langle x \rangle^2 = \frac{1}{s}\int_0^s x^2 dx - \left(\frac{1}{s}\int_0^s x dx\right)^2 = \frac{1}{3}s^2 - \frac{1}{4}s^2 = \frac{s^2}{12} \tag{VII.3}$$

So the standard deviation becomes $\sigma = \sqrt{Var(x)} = \frac{s}{\sqrt{12}}$. With a wire pitch of $s = 1.5$ mm the theoretical resolution of the chamber in x-direction is $\rho_x = 433\ \mu$m which fits very good to the mean value of the result from VII.2.

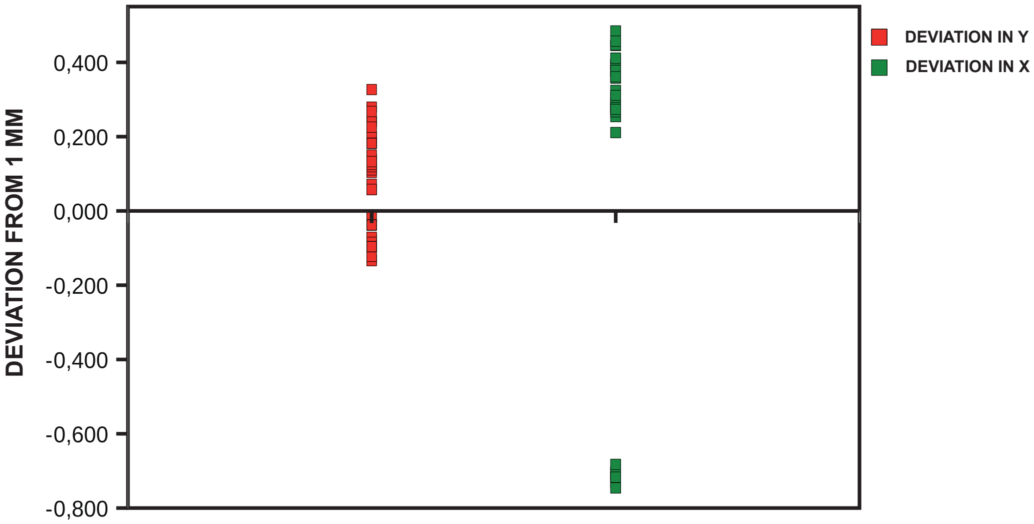

Figure VII.8: Deviations from the distance of the two measured peaks from one millimetre. The distance from the pin-holes centres of the collimator was one millimetre.

VII.5 Spatial Resolution

The spatial resolution of the MSPET prototype chamber was finally determined with the 200 μm, the 100 μm, and the 50 μm collimators. Six measurements for different positions were performed with the 200 μm collimator and three measurements with the 100 μm collimator. For the 50 μm collimator the number of photons which passed the collimator was so low that it was not possible to seperate them from the background. The results for the 200 μm collimator are shown in Figure VII.9 and Figure VII.10. The hit maps for the 100 μm collimator measurements are presented in Figure VII.11. Gaussian fits were applied to the projections to the wire direction of this data.

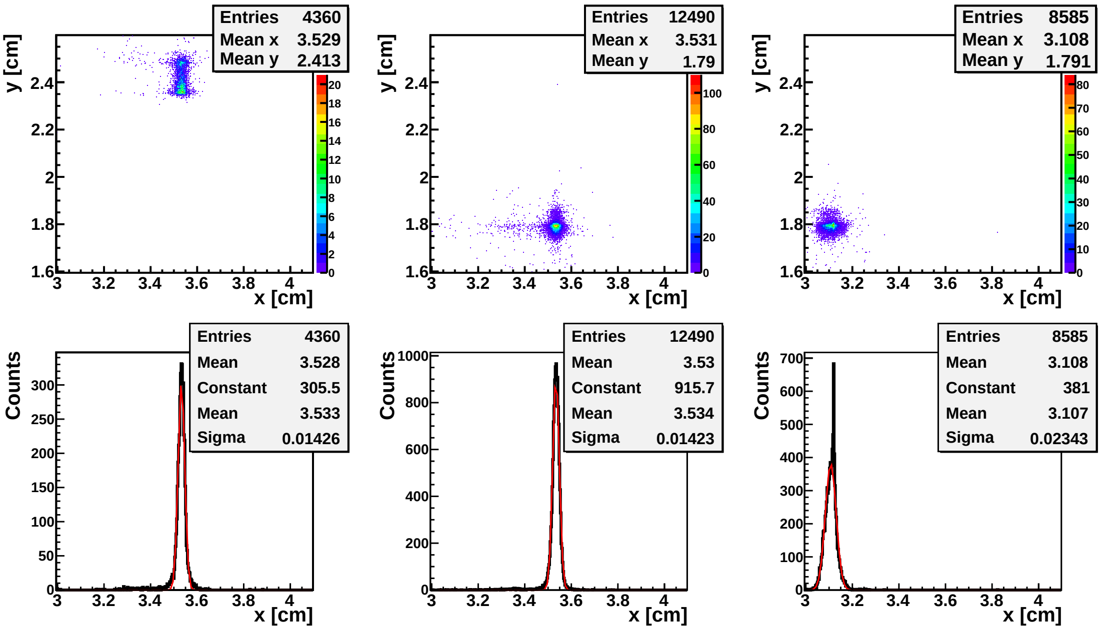

Figure VII.9: 2D hit maps from a measurement with the 200 μm collimator. The associated projections to the wire direction with Gaussian fits are shown in the lower row.

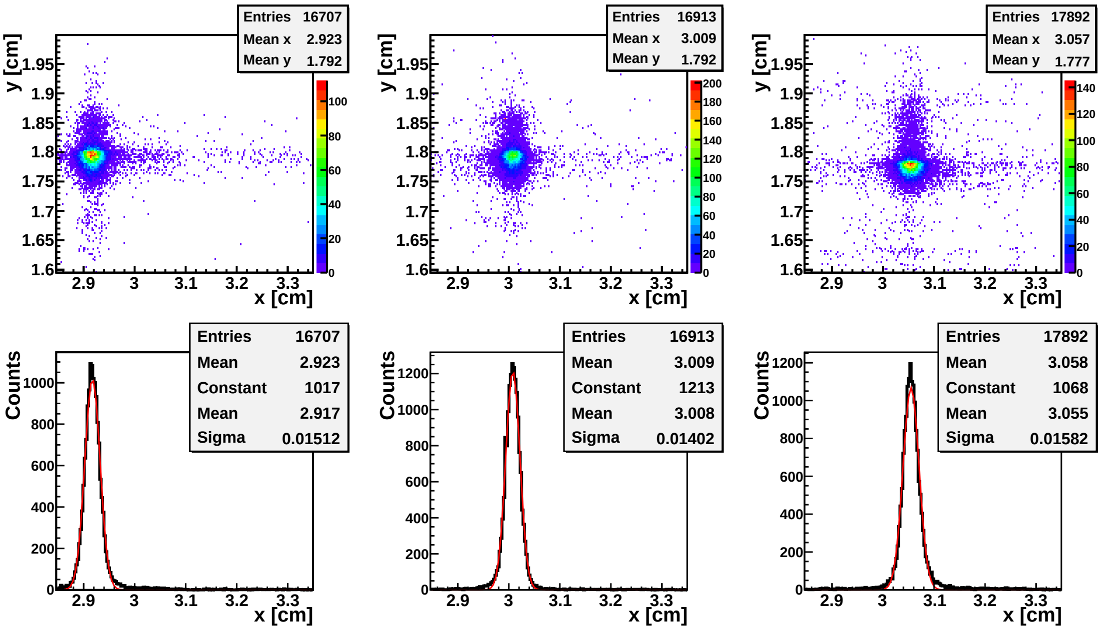

Figure VII.10: 2D hit maps from a measurement with the 200 μm collimator. The associated projections to the wire direction with Gaussian fits are shown in the lower row.

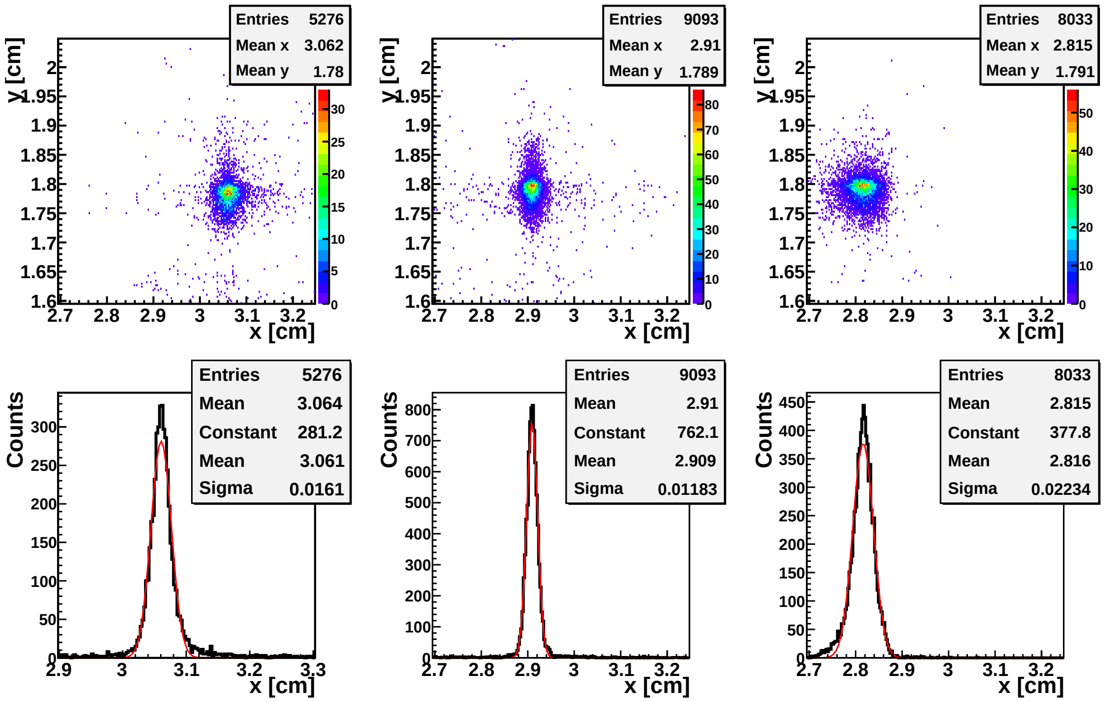

Figure VII.11: 2D hit maps from a measurement with the 100 μm collimator. The associated projections to the wire direction with Gaussian fits are shown in the lower row.

The average standard deviation from the six measurements with the 200 μm collimator and the average standard deviation from the three measurements with the 100 μm collimator are given by:

$$\begin{aligned} \sigma_{200\mu m} &= 161\mu m \pm 36\mu m \\ \sigma_{100\mu m} &= 167\mu m \pm 53\mu m \end{aligned} \tag{VII.4}$$

As the standard deviation is not increasing with the diameter size of the collimator, it is shown that the collimator diameters are low enough to treat the beam as a point source. Therefore, the spatial resolution is the spread around the centre of the peak, so that the standard deviation is an appropriate value for the spatial resolution in the direction parallel to the wire direction. The same procedure could not be applied in the direction perpendicular to the wires. Therefore, the spatial resolution in this direction cannot be determined exactly, but the measurements with the four pin-hole collimator let assume that the theoretical resolution of 433 μm can be reached.

As mentioned in section V.5, the anode cathode gap was reduced to one millimetre, so that the spatial resolution for annihilation photons which cause conversion electrons with an average exit angle of 45°, is in the order of one millimetre. As the spatial resolution for low energy X-rays is much smaller than a millimetre, the detector should be able to determine the position of conversion electrons with an accuracy of one millimetre.

VII.6 Difficulties in Determining the Spatial Resolution with other Methods

Several methods to determine the spatial resolution of the MSPET prototype chamber have been investigated. Out of these only the methods described above provide reasonable results. This section is designated to give some reasons whereas the other methods are not appropriate to determine the spatial resolution.

- A first attempt was to use a ^{22}Na source which was collimated with a three centimetre thick lead block with a one millimetre thin pin-hole. With this setup it was not possible to produce a defined beam of photons with an energy of $E = 511$ keV.
  The collimator was also used in a one millimetre thick slit setup. It was possible to reproduce a rough image of the slit in three different directions with the MSPET prototype chamber, but these measurements were not good enough to give information about the spatial resolution.

- Another attempt was to use a ^{55}Fe source which produces gamma rays with a mean energy of $E = 5.9$ keV. The measurements were not successful which is not a big surprise if one looks at the transmission curve for the copper layer in Figure VII.2. As the transmission for the gamma rays of the iron source is very low, measurements with the iron source are not reasonable.

- It was also tried to make measurements with the one millimetre pin-hole collimator of the X-ray source described in section VII.1. The spatial resolution of the chamber was determined by moving the beam in stages over the chamber. Thereby the reconstructed distance between two beam positions was compared to the applied displacement. The average deviation should then be an indicator for the spatial resolution. The average deviations from fifty measurements are:

$$\rho_x = 113\ \mu\text{m} \pm 83\ \mu\text{m} \qquad \text{and} \qquad \rho_y = 188\ \mu\text{m} \pm 119\ \mu\text{m}$$

Perpendicular to the wire direction the resolution is much lower than the theoretical prediction. This arises from the step-size of the detector movement. The detector was moved in 500 μm steps in both directions at the same time in this measurement. Therefore, the chamber was always irradiated at positions which had alternating the same distance to a wire. Thereby the measurement was not appropriate to determine the spatial resolution.

Assuming, that if the detector is moved in smaller step-sizes of e.g. 50 μm over the beam, the results would be adequate to determine the spatial resolution. But as the uncertainty of the chamber position is around $\sigma_{x,y} \approx 100\ \mu$m such a measurement was not possible with this measurement setup.

CHAPTER VIII

Measurements and Simulations

The detector response to annihilation photons and on low energy X-rays is different. This chapter shows and explains differences.

The second part of this chapter shows that the detector response to homogeneous distributed annihilation radiation shows an unexpected pattern. Simulations were performed which reveal the origin of this pattern.

VIII.1 Gas Gain

The avalanche multiplication factor called *gas gain* was treated theoretical in Section IV.2.3 and is an inherent attribute of a gaseous detector. A direct measurement of the gas gain is only possible if the number of primary ion pairs which are produced through the ionisation within the gas layer is known. For the MSPET prototype chamber and the radiation sources which were available, the exact number of primary ion pairs was not known. Therefore, it was more reasonable to determine only the pulse height distribution of the detector as the pulse height of the signal is proportional to the gas gain. The same measurement setup that was used to determine the spatial resolution, Section VII.2, could be used to determine the overall charge induced on the pads by an avalanche.

The MSPET prototype chamber was irradiated with the X-ray source without the collimator inlet which was shown in Figure VII.1. The high voltage was raised in 10 V steps and in each step the chamber was irradiated three minutes long.

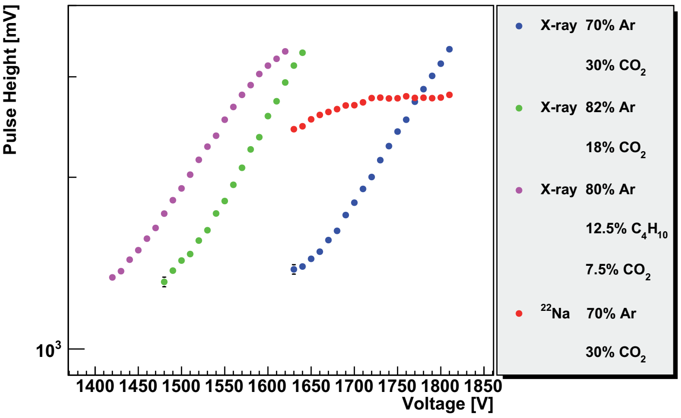

Figure VIII.1: The mean pulse height is a function of the applied voltage. The mean pulse height indicates the distribution of the gas gain which differs for signals produced by the X-ray source and the ^{22}Na source. The measurements with the X-ray source were performed for three different gas mixtures.

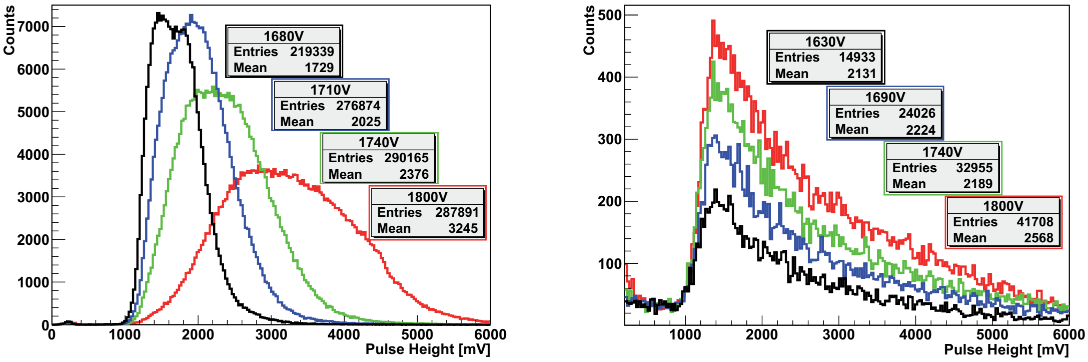

(a) (b)

Figure VIII.2: In both figures the histograms of the pulse height distribution of the signals for four different voltages are presented. In figure (a) the signals were produced by the X-ray source whereas figure (b) presents the signals induced by a ^{22}Na source. In both measurements a gas mixture with 70% Ar and 30% CO_2 was used.

The measurements were performed for three different gas mixtures. The same measurement was also performed with a ^{22}Na source. The source was mounted directly in the front of the chamber. This was performed only for one gas mixture.

The pulse heights of each cathode pad were summed up for each cathode plane in every event and filled in a histogram.

With this histogram the average pulse height for each voltage step was determined.

The results are shown in Figure VIII.1. The average pulse height is plotted in a logarithmical scale, so that the exponential dependence on the voltage for the X-ray source which is suggested theoretical and by simulations with Garfield [Got09], can be validated.

Figure VIII.2 compares four histograms of the pulse height distribution between the ^{22}Na and the X-ray source. The distributions for the X-ray source in (a) represent the energy spectrum of photons for different gains and the curve progression is as expected. In (b) the avalanches are produced by conversion electrons with energies with a distribution around approximately 280 keV. It seems that it was not possible to obtain the full spectrum of the conversion electrons. Therefore, more measurements with different gas mixtures are needed to investigate, if it is possible to detect the full conversion electron spectrum with the MSPET prototypes.

VIII.2 MSPET Prototype Chamber Response on Annihilation Radiation

The response of the MSPET prototype chamber to annihilation radiation differs to the response to X-rays which was shown in Figure VII.5. A difference is that the 511 keV annihilation photons are not absorbed by the detector frame or the cathode pads and, therefore, the gas layer is irradiated homogeneously. Another difference is that the electrons which are liberated from the cathode pads or which are produced by interaction in the gas layer have a larger scattering angle and a higher energy. Therefore, it is possible that the avalanche occurs at one, two or even at three or more wires at the same time. For the X-ray photons in contrast the avalanche will occur mainly on one wire. Sketches of the different ionisation processes are illustrated in Figure VIII.3.

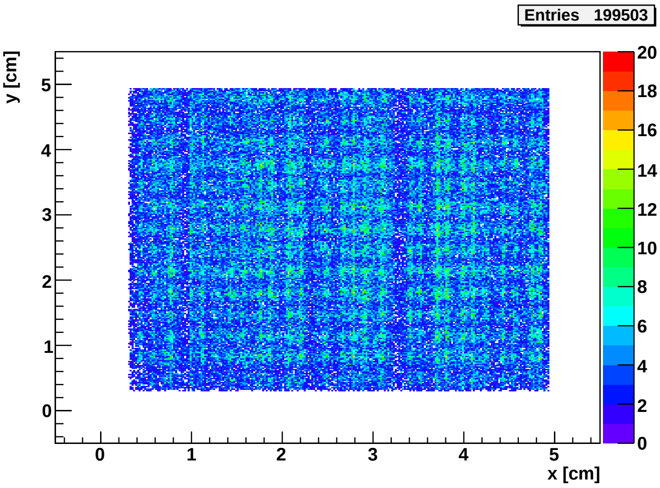

Figure VIII.4: 2D reconstruction of avalanche positions within the MSPET prototype chamber. The chamber was irradiated with a ^{22}Na source which was mounted five centimetre in front of the chamber, so that the chamber was homogeneously irradiated.

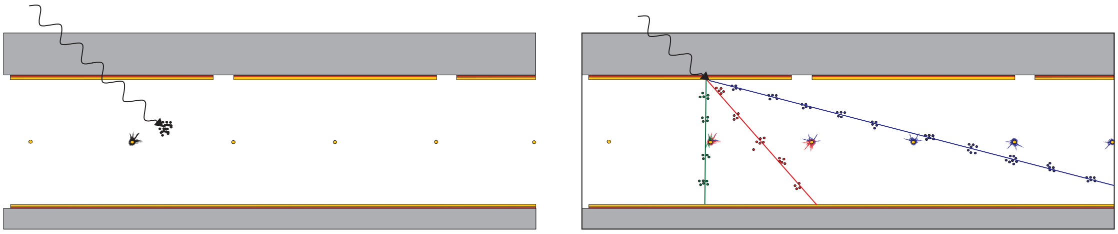

(a) (b)

Figure VIII.3: Comparisons of the ionisation processes within a MSPET prototype for low energy X-ray photons (a) and annihilation radiation (b).

The reconstruction of the avalanche positions in two dimensions for a MSPET prototype chamber which was irradiated with a ^{22}Na source is shown in Figure VIII.4. The avalanche positions were reconstructed with the unweighted displacement function Equation V.17. The associated projections on the y- and x-axis are illustrated in Figure VIII.5. Subfigure (a) shows the reconstruction in the direction perpendicular to the wires. Therefore, the distribution should be homogeneously. The peak structure within the distribution indicates that errors originate in position reconstruction so that hits pile up in the middle of each pad. The reasons for this problem will be topic of the next section. The projection to the axis in Subfigure VIII.5(b) shows peaks at the wire positions which is expected. By comparing the projection with the measurement with the X-ray source in

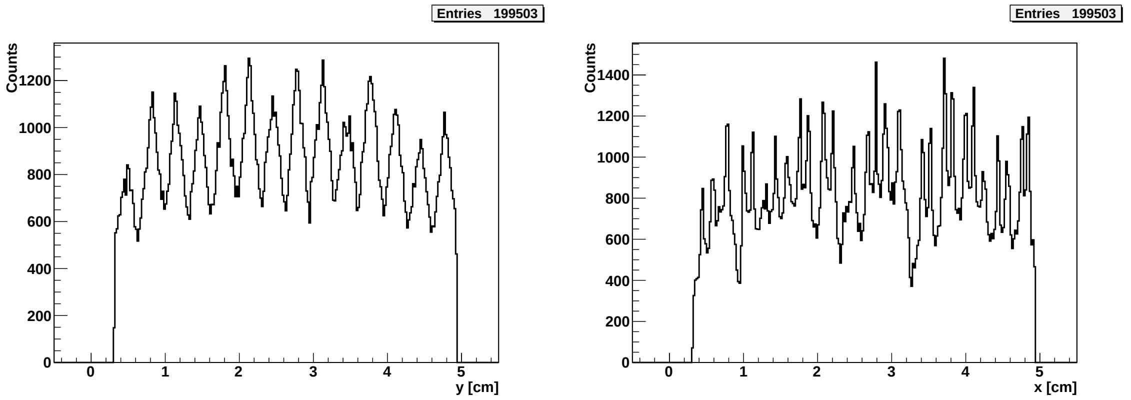

(a) (b)

Figure VIII.5: Projection on the y-axis (a) and x-axis (b) from the avalanche positions of the chamber, which was irradiated with a ^{22}Na source. The associated 2D plot is shown in Figure VIII.4. (a) shows that a reconstruction with the unweighted displacement function leads to an inhomogeneous distribution. In Figure (b) the wire arrangement dominates the position of the avalanches.

Figure VII.5, one sees that there are much more continuously distributed avalanche positions when the chamber is irradiated with the ^{22}Na source. This comes up as a conversion electron can produce avalanches on multiple wires at the same time.

A common way to determine the PRF-σ for the weighted displacement function Equation V.20 is to plot the reconstructed displacement from the centre of the pad with maximum charge against the ratio of the charge on one pad of the three participating pads to the overall charge into a two dimensional histogram. In the following this plot will be called *pad response function plot* (PRF-plot). The PRF-plots for measurements with the ^{22}Na source and the X-ray source are shown in Figure VIII.6. The theoretical distribution of the PRF can be calculated with Equation V.12 and is plotted as pink curve into the two dimensional histograms. The measured data follows the theoretical distribution, but the deviations around this distribution are relatively large which occurs due to the small dimensions of the prototype chamber. By comparing the two plots in Figure VIII.6, one sees that the hits disperse stronger for the ^{22}Na source. The charge ratio reaches values up to 0.3, which means, that the charge on all three pads was the same.
This comes up when the signal was induced on multiple wires.

One has to recognize that the theoretical PRF function is derived for avalanches occuring on only one wire.

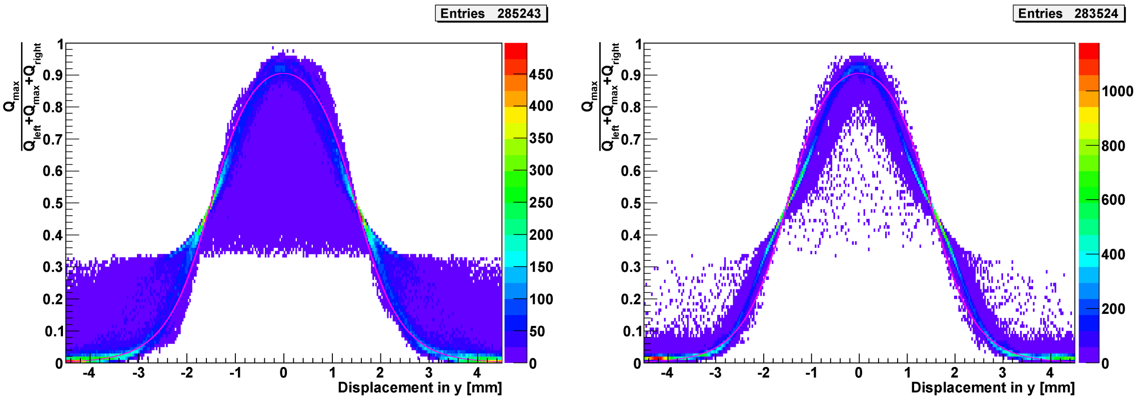

(a)

(b)

Figure VIII.6: Displacement from the centre of the pad which carries the maximum charge against the charge ratio. Figure (a) shows the distribution for the ^{22}Na source. The data points disperse around the ideal distribution, which is given by equation V.12 and plotted as pink curve. The same distribution for the X-ray source is displayed in Figure (b). One sees that the deviations are much larger for the ^{22}Na source than for the X-ray source.

VIII.3 PRF-Simulations

In Figure VII.5 and Figure VIII.5 it was shown that the reconstruction of avalanche positions contains unexpected artefacts. Therefore, it was decided to perform PRF-simulations to investigate if the chosen geometry for the MSPET prototype chamber is able to provide appropriate avalanche position reconstruction. The simulation was realised by a two dimensional grid which equated the cathode layer. The charge induced on the copper layer by the avalanche was simulated as a two dimensional Gaussian distribution. The average value of the Gaussian distribution was created randomly. The random values also followed a two dimensional Gaussian distribution in order to simulate a beam. For each event the grid was splitted into nine pads with the geometry of the pads from the MSPET prototype chamber and all pixels within a pad were summed up and built the charge value of the pad. In Figure VIII.7 and Figure VIII.8 the result of the simulation is presented.

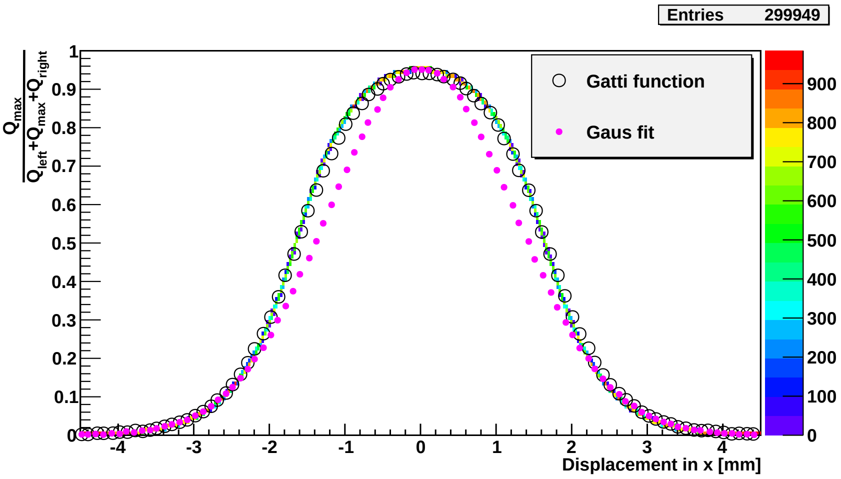

Figure VIII.7: PRF plot from simulated data. The black cycles show that the theoretical prediction from the Gatti formula follows the progression of the simulated data. The pink points represent a Gaussian fit to this data. The fit describes just a rough estimation of the real curve progression.

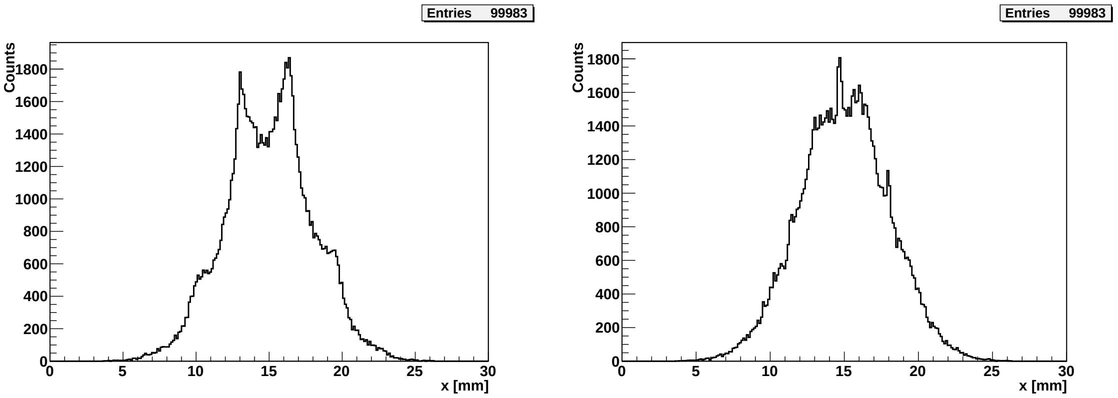

(a) (b)

Figure VIII.8: Reconstruction from the simulated data of Figure VIII.7. Figure (a) illustrates that the reconstruction with the unweighted displacement function shows a deformed image of the input distribution. A reconstruction with the weighted displacement function where the PRF-σ was taken from the Gaussian fit in Figure VIII.7, in contrast, is able to deliver an appropriate image of the input distribution which is shown in figure (b).

The σ for the Gaussian distribution which simulated the charge on the whole cathode layer was chosen to be $\sigma = 0.9$ mm. Figure VIII.7 shows that this was an appropriate value as the theoretical distribution, represented as black cycles, has

the same progression as the simulated data.A Gaussian fit was applied on this data and the progression is displayed as pink dots in the plot. One should realize that the data does not follow a Gaussian distribution anymore.
Position reconstruction for this simulated data are presented in Figure VIII.8(a) and (b). Where in (a) the reconstruction was performed with the unweighted displacement function and in Figure (b) with the weighted displacement function where the PRF-σ was determined with the Gaussian fit in VIII.7. The progression in Figure (b) represents the Gaussian distribution of the beam shape which was simulated with only tiny artefacts. The reconstruction in (a) with the unweighted displacement function in contrast produces undesired artefacts.
To be able to distinguish simulations with measured data, it is necessary to analyse in how far and in which form the measured data differs from the theoretical values. For the analysis of this behaviour two datasets, one from the ^{22}Na source measurements and one from the X-ray source measurements, have been studied. For each event the charges of the three most significant adjacent pads were plotted and a Gaussian fit was performed to this three data points. The σ of the fit was then filled in a histogram. The results for both datasets are shown in Figure VIII.9. In Figure (a) the σ distribution for the ^{22}Na is presented. The progression can be described by a landau distribution which is plotted in red.

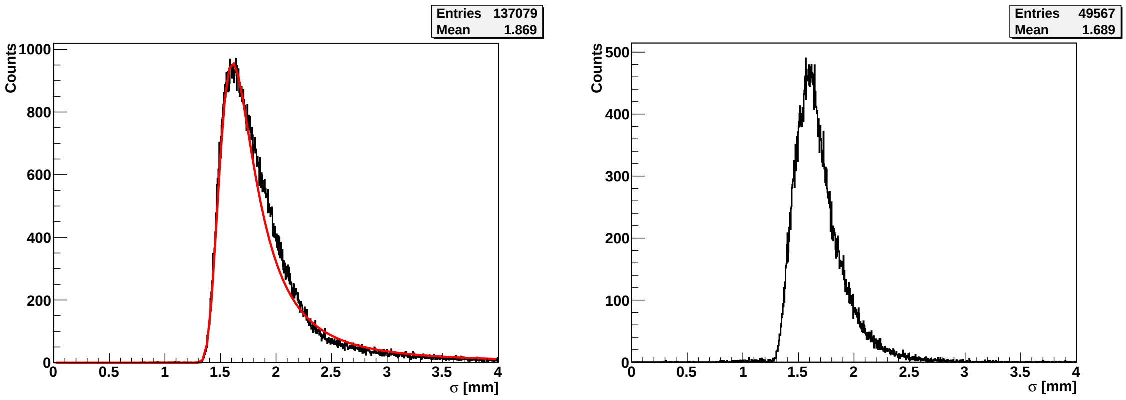

(a) (b)

Figure VIII.9: The plots show PRF-σ-distributions where each PRF-σ was derived from a Gaussian fit on the charge values of three adjacent pads from a single event. In Figure (a) the MSPET prototype chamber was irradiated with a ^{22}Na source. The landau distribution shown in red is appropriate to describe the curve progression. In Figure (b) the chamber was irradiated with the X-ray source.

The progression of a landau distribution comes up from large exit angles of conversion electrons. The probability for large exit angles is low, but when they occur they produce large PRF-σ's. The distribution shown in Figure VIII.9(b) was obtained from the X-ray data and is not landau distributed.
As the dispersive behaviour of the PRF-σ was known then, it could be implemented in the simulations. The simulation of the ^{22}Na source response was performed by assigning the PRF-σ to the two dimensional Gaussian distribution which simulated the charge induced on the cathode layer as random values which were landau distributed.
A comparison of simulated with measured data is illustrated in Figure VIII.10.The parameters for the random landau distribution were set to $\sigma = 0.077$ and MPV=0.9 [1]. In Figure VIII.10(a) and (b) the PRF plot and the position reconstruction for simulated data are presented. The beam width was made very broad to compare the data with measurements where the source irradiated the chamber homogeneously. In figure (c) and (d) the associated measured data which was also shown before is presented. The histogram in (d) is thereby zoomed to the first nine pads, so that the plots can be compared directly. The PRF plots show that the simulation is appropriate and we obtain similar artefacts in the simulation and the measurement. However, it is pointed out that the peak pattern is more pronounced in the measured data. A possible reason could be that the simulation did not consider any noise in the data.
The position reconstruction was performed with the unweighted displacement function. Reconstructions with the weighted displacement functions showed images with more artefacts disregarding which value for the PRF-σ was designated.

The deviation from the theoretical PRF to a Gaussian distribution shown in Figure VIII.8 can be reduced by downsizing the pad width or enlarging the anode-cathode gap. Figure VIII.11 shows the simulated response for a MSPET prototype chamber, where the pad width is reduced to 2.1 mm or the anode-cathode gap is enlarged to 1.3 mm, on annihilation radiation. One can see that the reconstruction artefacts are minimized. The simulation of such geometries showed better reconstruction results but these geometries have unsatisfying drawbacks. A larger anode-cathode gap would diminish the spatial resolution due to the correlation to the exit angle of the conversion electrons.

---

[1] MPV= Most probable value

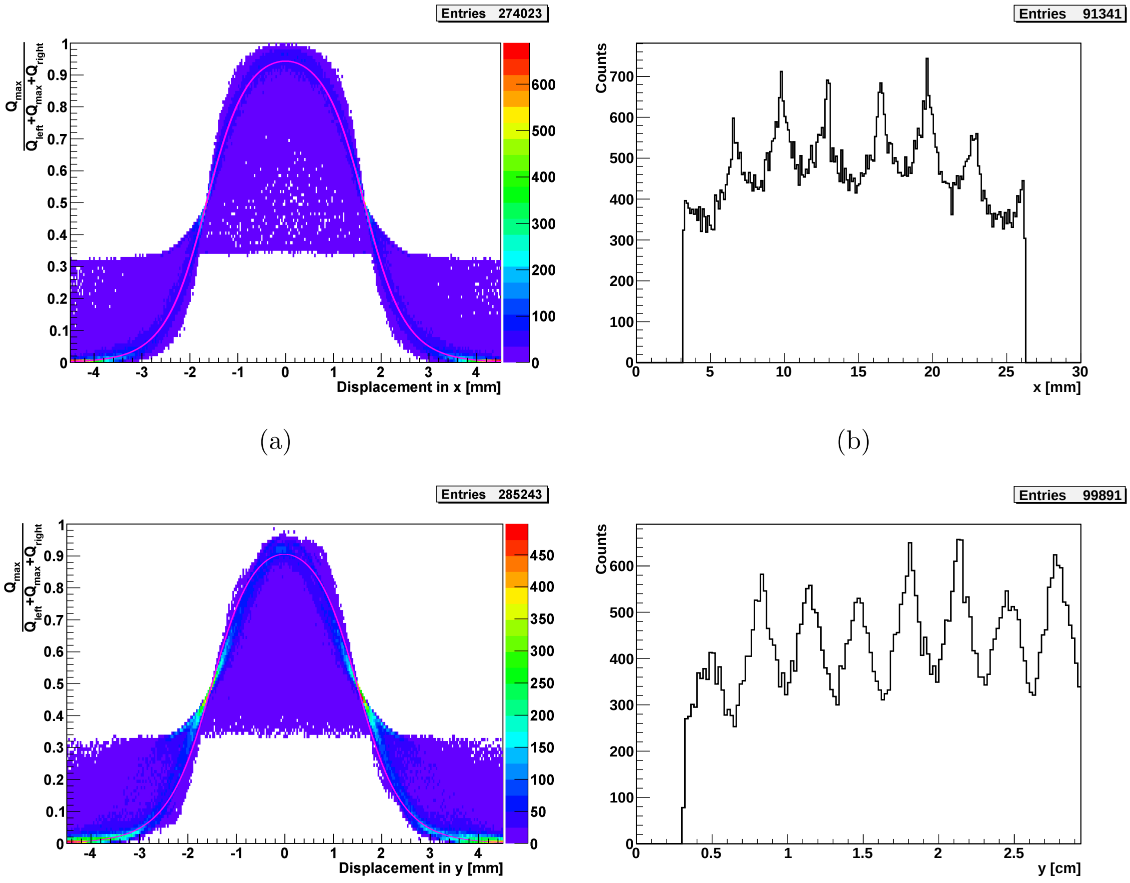

(a) (b)

(c) (d)

Figure VIII.10: Comparison of simulated and measured data. Figures (a) and (b) show simulated data where the simulation shown in Figure VIII.7 was smeared with the PRF-σ distribution shown in Figure VIII.9(a). Figures (c) and (d) show the measured data of a ^{22}Na source. In Figure (a) and (c) the PRF plots are compared. In Figure (b) and (d) the associated position reconstructions are compared. The same peak pattern is given in the simulation and in the measurement. However, the peak structure in the measurement is more pronounced.

On the other hand a reduction of the pad width implies the need for more read out channels and the construction of the converter pads becomes more complicated. Therefore, it was decided to retain the old geometry as the error due to the reconstruction is smaller than the desired spatial resolution for the tomograph.

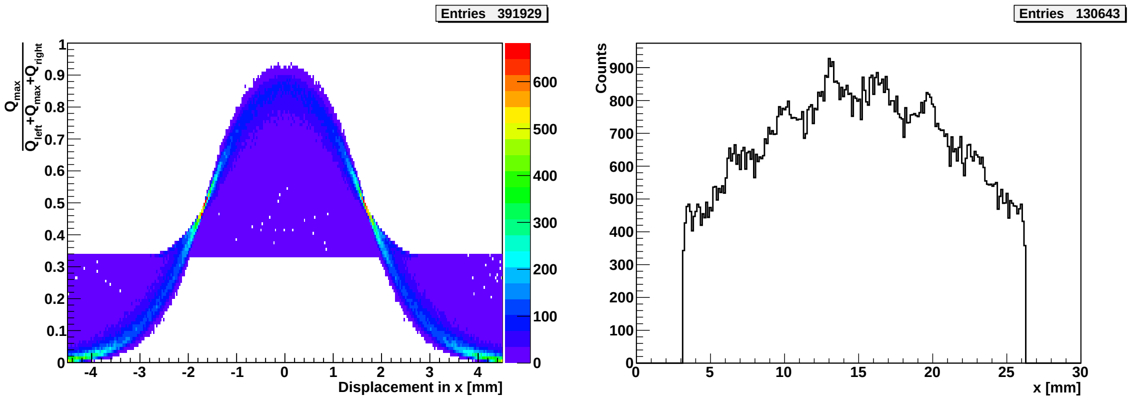

(a) (b)

Figure VIII.11: Simulations for a MSPET prototype chamber with smaller pads or larger anode-cathode gap. They show that the peak pattern in the position reconstruction can be reduced, so that the pattern disappears almost entirely.

CHAPTER IX

Gold Converter and PET Measurements

This chapter shows measurements which were performed with a MSPET prototype chamber which was upgraded with a gold converter. It presents also first PET measurements. From the event numbers of these measurements it is possible to calculate the efficiency to detect annihilation radiation in two different ways.

IX.1 Measurements with a Prototype that had a Gold Converter

A printed circuit board with copper pad structure was sent to the company *Drollinger*. They electroplated the copper pads with a gold layer. A gold layer with a thickness of thirty micrometres was ordered. A determination of the weight of the circuit board, before and after the electroplating process, resulted in an average thickness of sixty micrometres. Measurements with a 3D probe head showed that the thickness was varying from 30 to 120 micrometres for different positions on the pads.

Nevertheless, a MSPET prototype chamber was constructed with this gold converter layer. The gold prototype provided stable operation, although the cathode pads had an unsteady gold layer.

The prototype chambers showed a unsteady pattern for reconstructed avalanche positions when they were irradiated homogeneously with a ^{22}Na source. This was treated in Chapter VIII.2 and an example hit map was shown in Figure VIII.4.

Similar images were obtained with the gold prototype. We did not obtain an unsteady production of conversion electrons which was expected due to varying converter thicknesses and the reconstruction artefacts were still present.

Count rate measurements were also performed with the ^{22}Na source for the gold converter prototype chamber and for the prototype chamber without gold converter. In both measurements the chambers were irradiated with the ^{22}Na source for five minutes where the source was mounted directly in front of the chambers. The results are presented in Figure IX.1. One can see that the count rate obtained with the gold converter chamber is approximately 30% higher at the maximal applicable voltage than the count rate of the chamber without gold converter.

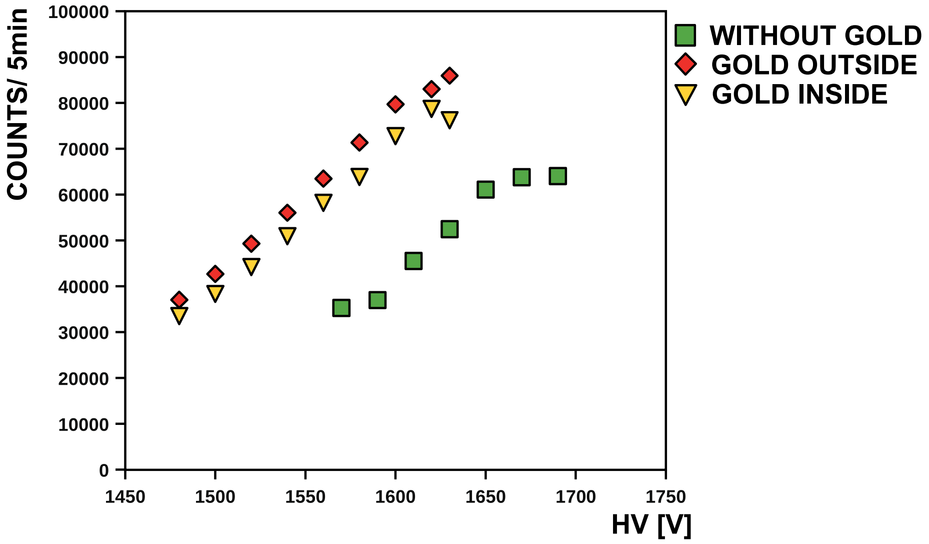

Figure IX.1: Count rate performance of two different MSPET prototype chambers irradiated with a ^{22}Na source. The cathode layer of one chamber was covered with a gold layer which acts as converter. The chamber with gold converter could be irradiated from two different sides as just one cathode layer was electroplated with gold. The red rhombs were from a measurement where the gold converter was on the outer cathode layer so that the photons penetrated the converter after passing the gas layer. The yellow triangles were from a measurement where the gold converter was on the inner cathode layer so that the photons penetrated the converter directly. In this case the photons did not had to pass the gas layer.

GEANT4 simulations for a MSPET scanner were performed by H. Gottschlag [Got10]. They were made for a MSPET scanner that consisted of 200 detectors which were subdivided into four stacks. These stacks were arranged

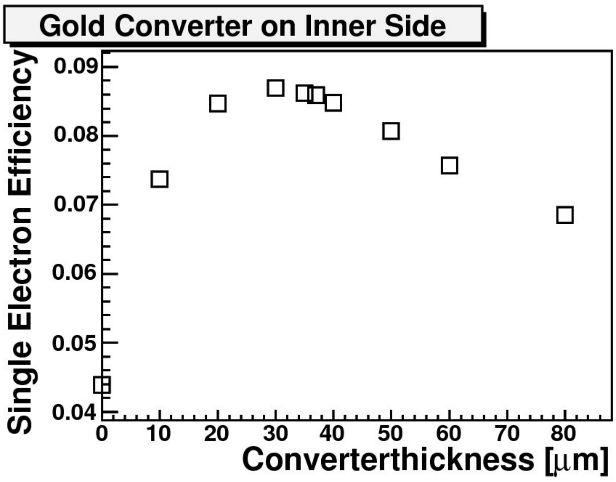

Figure IX.2: Simulations of the singles efficiency in a MSPET scanner. The simulated scanner consisted of four stacks with 50 detectors each. The singles efficiency to detect 511 keV photons was simulated with varying gold converter thicknesses [Got10].

symmetrically around the centre of the FOV. The simulations were made with varying converter thicknesses and performed for gold and lead converters. The single electron efficiency for a scanner which contains detectors with a gold converter on the inner pad plane is shown in Figure IX.2.

One sees that the optimal converter thickness for a gold converter is around thirty micrometres. For this converter thickness the singles efficiency is doubled if one compares it with the singles efficiency of a gold converter with a thickness of zero.

As the gold converter had an average thickness of sixty micrometres in the measurements, one would expect that the count rate would be increased by approximately 80% following these simulations.

A difference between the simulations and the measurements is that the simulation provides an ideal source where the number of emitted photons is exactly known. The ^{22}Na source which was used in the experiment produces, additionally to the annihilation radiation, a 1275 keV photon in each decay. It is also possible that Bremsstrahlung occurs in the ^{22}Na source as a thin stainless steal foil is in front of the source. When the positron from the β^+-decay is decelerated in this stainless steal foil, it is possible that Bremsstrahlung is generated.

The observation that the simulations and the measurements cannot be directly compared can also be seen in Figure IX.1. The chamber with gold converter can be irradiated from two different sides as just one cathode layer was electroplated with gold. The red rhombs in Figure IX.1 were from a measurement where the gold converter was on the outer cathode layer so that the photons penetrated the converter after passing the gas layer.

The yellow triangles were from a measurement where the inner cathode layer had the gold covering so that the photons penetrated the converter directly. In this case the photons did not had to pass the gas layer.

We observed that the count rate is approximately 10% higher for the red rhombs. From simulations it is known that the count rate should be lower for the red rhombs.

Therefore, it is necessary to repeat these measurements with a different source which is not collimated with high Z material. Such a source would not produce Bremsstrahlung. On the other hand more prototype chambers with a converting material of precise thickness are needed to obtain correct and comparable results.

IX.2 PET Measurements

IX.2.1 Measurement Setup

The first real PET measurements were made with a prototype chamber without gold converter and a prototype chamber with gold converter. For these measurements only 44 pre-amplifiers (PNG CATSA) and main amplifiers (PNG MA8000) were available. Therefore, each chamber had only eleven active read out channels for each direction. With a pad width of three millimetre, a gap of 0.3 mm, and the disadvantage that the two end pads did not contribute to the active detection area,[1] it was only possible to obtain an active detection area of 2.97×2.97 cm^2 per detector.

For the PET measurements the chamber carrier which was used for the spatial resolution measurements was upgraded. This time the carrier was used as a source holder. The two chambers were arranged face to face in a distance of nine centimetres on two new fixed chamber carriers. Therefore, the source could be moved precisely in the plane parallel to the detectors and was fixed in the direction perpendicular to the detector surface. Thus, the source was always three centimetres away from detector one and six centimetres away from detector two. In Figure IX.3 a sketch of the measurement setup from two perspectives is shown.

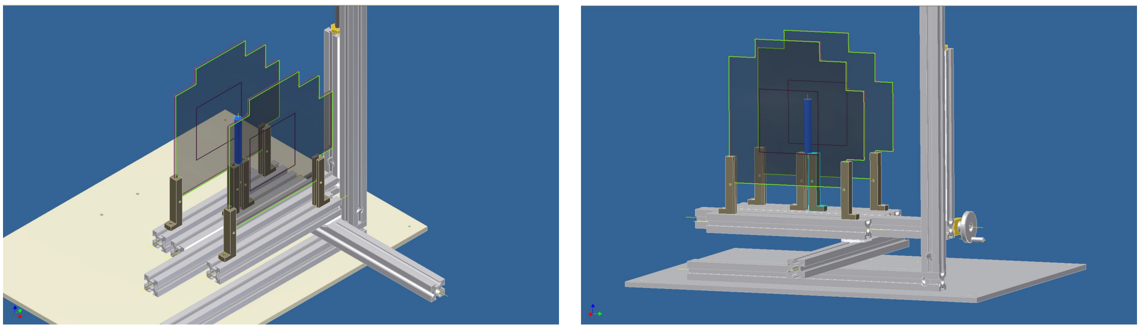

Figure IX.3: Technical drawings from the setup of the PET measurements from two perspectives done by W. Verhoeven. The blue cylinder illustrates the sodium source.

The electronic setup for the read out was closely related to the electronic setup which was used in the spatial resolution measurements shown in Figure VII.3.

---

[1] With the charge dividing read out method three adjacent pads are needed. The two end pads have only one neighbour each. Therefore, they cannot contribute to the active read out area.

The number of readout channels for one chamber was reduced from 32 to 22 and the gate for the ADCs was then generated from the wire signals of both chambers. This means that the wires of each chamber were connected to two separated pre-amplifiers[1]. A logic OR gate[1] was used to combine the two signals after the P/S delay generator. Therefore, the ADCs digitised the signals on all channels when a signal was induced on the wires of at least one chamber. The high voltage of each chamber was produced by two ISEG high voltage power supplies which were monitored by two separate PCs.
The data from the peak sensitive ADCs was read out and stored as ASCII files by a C program. The data was later converted into a *ROOT*-file [BR97]. A *ROOT*-macro filtered the coincidences out of this data and stored the coordinates of the reconstructed positions of the avalanches in both chambers in a binary-file.
The image reconstruction was then performed by an *expectation maximisation - maximum likelihood* (EM-ML) algorithm which has been implemented in a C program by T. Kösters [Kö09].

IX.2.2 Image Reconstruction of a Sodium Source

The reconstructed images of three single measurements using a sodium source are shown in Figure IX.4. The sagittal slice shows the plane in which the source was moved. One can see that the source was placed at three different positions.

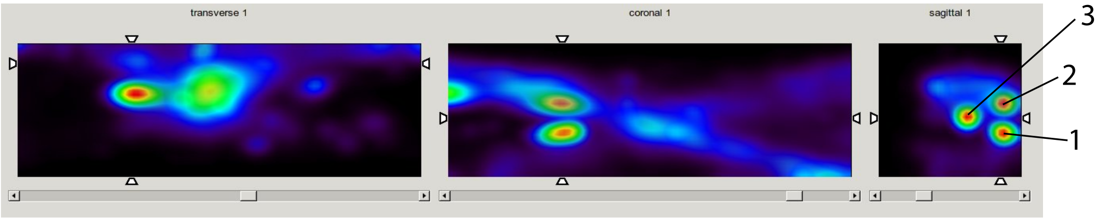

Figure IX.4: EM-ML reconstruction of the ^{22}Na source. The source was moved to three different positions in the FOV. The LORs were measured with two MSPET prototype chambers. The reconstructed image positions of the source matched to the applied displacements of the source. The shape of the reconstructed image of the source does not correspond to the expectation.

---

[1] One pre-amplifier and the logic OR gate were constructed by the IKP workshop. The pre-amplifier was needed to be able to trigger on both chambers at the same time. It was necessary to built one as no second ORTEC Model 124 pre-amplifier was available.

Measurement No.	Measurement time [h]	No. of valid coincidences
1	111	523
2	137	8257
3	68	10108

Table IX.1: Measurement time and number of valid coincidences for three measurements with a ^{22}Na source at three different positions. The measurement number corresponds to the labels in Figure IX.4. The number of valid coincidences increased strongly as the source was moved more and more to the centre of the FOV.

The applied displacements of the source match to the reconstructed displacements. The numbers at the reconstructed sources in Figure IX.4 indicate the associated measurements. The measurement time and the number of measured coincidences are shown in Table IX.1.

Unfortunately, it was not possible to obtain the shape of the sodium source which has the form of a coin with a diameter of three millimetre and a height of one millimetre. This can be caused by the small solid angle which was covered by the two detectors and the low statistics of the data. Therefore, the given measurement setup was not able to determine the spatial resolution for the intended MSPET scanner.

In order to be able to determine the spatial resolution more readout electronics, a smaller source with a higher activity, and maybe a stack of several detectors are needed.

Nevertheless, these first PET measurements showed that the detectors are able to provide PET images where the position of the source can be reconstructed.

IX.2.3 Efficiency to detect Annihilation Radiation

There are two ways to determine the efficiency to detect photons with an energy of $E = 511$ keV with a PET measurement where the source is placed in the middle of the field of view. Figure IX.5 shows a measurement where it was possible to place the source approximately in the centre of the FOV. The number of events in this measurement are noted in Table IX.2. In this case valid coincidence means that in both detectors was a signal with a pulse height between two thresholds.

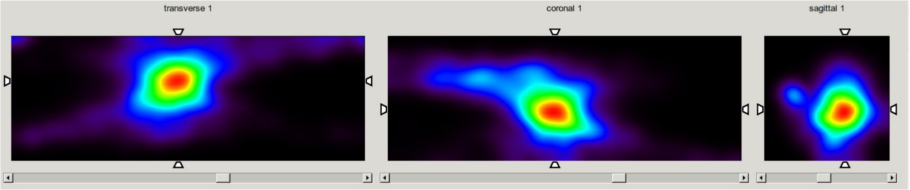

Figure IX.5: Reconstruction of a PET measurement where the sodium source was placed in the centre of the FOV.

No. of valid coincidences	4500
No. of valid singles detector 1	961060
No. of valid singles detector 2	1289803

Table IX.2: Number of events in a PET measurement with a ^{22}Na source in the centre of the field of view. Detector one is the chamber with gold converter and detector two is the chamber without gold converter.

The whole measurement took 68 hours. As one assumes that every single signal induced in one detector is originated by a 511 keV photon and the source was exactly in the centre of the both detectors one can calculate the efficiency of one detector by dividing the number of valid coincidences by the number of valid singles of the other detector:

$$\begin{aligned} N_{Co}/N_{si2} &= \frac{4500}{1289803} = 0.349 \pm 0.005\% \\ N_{Co}/N_{si1} &= \frac{4500}{961060} = 0.468 \pm 0.007\% \end{aligned} \tag{IX.1}$$

Another way to obtain the efficiency of the detector is to divide the number of measured signals by the number of photons which crossed the detector. The ^{22}Na source had an activity of 47 kBq. Since the source was not calibrated the manufacturer gave an uncertainty of 40 %.

To calculate the solid angle which was covered by the detector one can assume in first approximation that the active detection area of the detector was on a surface of a sphere. As the surface of the whole sphere is given by 4π, one can calculate the proportion on the whole solid angle with:

$$\frac{\Omega}{4\pi} = \frac{A}{4\pi r^2} = \frac{(2.97)^2}{4\pi(4.5)^2} \approx 3.47\% \tag{IX.2}$$

As the measurement took 68 h $\widehat{=}$ 244800 s and each decay results in two photons[2], the number of photons which cross the active detection area becomes:

$$N_\gamma = 2 \cdot 47000 \cdot 244800 \cdot 0.0347 = 7.98 \cdot 10^8 \tag{IX.3}$$

Therefore, the efficiency of the both chambers is given by:

$$\begin{aligned} N_{si1}/N_\gamma &= \frac{961060}{7.98 \cdot 10^8} = 0.12 \pm 0.05\% \\ N_{si2}/N_\gamma &= \frac{1289803}{7.98 \cdot 10^8} = 0.16 \pm 0.06\% \end{aligned} \tag{IX.4}$$

By comparing the results from IX.1 with the results from IX.4 one obtains a discrepancy by a factor of around three.

For a large amount of random coincidences the results would be in better agreement, but with a coincidence window of ten microseconds and Equation III.3 one would expect only eight random coincidences in the whole measurement. So the random coincidences can be neglected.

If one would reject an expected amount of signals which could be produced by 1275 keV photons, Bremsstrahlung or sparking of the chamber, the discrepancy between the results would grow further.

Therefore, the discrepancy has to come up from data processing or misarrangement of the source. At this point further measurements will be needed to determine the efficiency to detect annihilation radiation.

---

[2] The decay of ^{22}Na results in the emission of three photons, but the probability to detect the 1275 keV photon with the prototype chamber is very low.

CHAPTER X

Conclusion

The MSPET prototype chambers were able to detect over 80% of the cosmic muons with differently applied gas mixtures. Therefore, the detectors should be able to detect the majority of conversion electrons which are caused from annihilation radiation.
The spatial resolution for low energy X-ray photons was measured to 161 ± 36 μm in wire direction and 432 ± 171 μm in the direction perpendicular to the wires which is in accordance with the theoretical expectations. Therefore, the prediction for the spatial resolution for annihilation radiation of one millimetre seems to be adequate.
The PET measurements have presented the ability of the chamber to detect annihilation radiation in a reasonable way and gave first approaches to calculate the efficiency. Unfortunately, it was not possible to determine the spatial resolution for annihilation radiation out of these PET measurements.
The first usage of a converting material showed that the detector response stays the same in such way that measured events had the same pattern when reconstructed and inhibited the same pulse height distributions. It was presented that the number of conversions is enlarged by using a converting material.

The next steps should be to build up more prototype chambers with converting materials of precise thickness and to produce adapted read out electronics. With more adapted readout electronics it will be possible to measure with sources which have a higher activity. This will open the opportunity to determine the

spatial resolution of the detectors to detect annihilation photons and to determine the efficiency correctly.
Also further measurements with different gas mixtures with consideration of pressure and flow should be established to determine the conditions which provide the most advanced detector performances.

Bibliography

[A^+08] C. Amsler et al. *Phys. Lett.* **B667** (2008) 1.

[All69] O. Allkofer. *Spark Chambers*. Thiemig, 1969.

[Bau09] C. Baumann. *private communication*, 2009.

[BCZC05] M. Berger, J. Coursey, M. Zucker et al. *National Institute of Standards and Technology, ESTAR*, August 2005. `http://physics.nist.gov/cgi-bin/Star/e_table.pl`.

[BR94] W. Blum and L. Rolandi. *Particle Detection with Drift Chambers*, Vol. 1st Edition. Springer, 1994.

[BR97] R. Brun and F. Rademakers. *Nucl. Instr. and Meth.* **A389** (1997) 81. `http://root.cern.ch/`.

[Bro59] S. Brown. *Basic data of plasma physics*. MIT Press, 1959.

[BRR08] W. Blum, W. Riegler and L. Rolandi. *Particle Detection with Drift Chambers*, Vol. 2nd Edition. Springer, 2008.

[BWW01] K. Bethge, G. Walter and B. Wiedemann. *Kernphysik*. Springer-Verlag, 2001.

[CD06] S. Cherry and M. Dahlbom. *PET:Physics, Instrumentation and Scanners*. Springer-Verlag, 2006.

[Cha72] G. Charpak. *Filet a particules*. Decouvertes, 1972.

[GLOS79] E. Gatti, A. Longoni, H. Okuno et al. *Nucl. Instr. and Meth.* **163** (1979) 83.

[Got09] H. Gottschlag. *private communication*, 2009.

[Got10] H. Gottschlag. *Small Animal Positron Emission Tomography with Multi-Wire Proportional Counters*. Dissertation, Institut für Kernphysik, 2010.

[Gru06] C. Grupen. *Physik in unserer Zeit* **16** (2006) 69.

[Hei53] W. Heitler. *The Quantum Theory of Radiation*, Vol. Third Edition. Oxford University Press, 1953.

[Hü07] H. Hünteler. *Development and Evaluation of a Multiwire Proportional Chamber for a High Resolution Small Animal PET Scanner*. Diplomarbeit, Institut für Kernphysik, 2007.

[Jac75] J. Jackson. *Classical Electrodynamics*, Vol. Second Edition. John Wiley and Sons, 1975.

[KB09] M. Klein-Boesing. *Development of a Transition Radiation Detector and Reconstruction of Photon Conversions in the CBM Experiment*. Dissertation, Institut für Kernphysik, 2009.

[Kle92] K. Kleinknecht. *Detektoren für Teilchenstrahlung*. Teubner, 1992.

[Kno79] G. F. Knoll. *Radiation Detection and Measurement*. John Wiley and Sons, 1979.

[Kor46] S. A. Korf. *Electron and Nuclear Counters-Theory and Use*. Van Nostrand Company, 1946.

[Kö09] T. Kösters. *private communication*, 2009.

[Leo87] W. Leo. *Techniques for Nuclear and Particle Physics Experiments*. Springer-Verlag, 1987.

[LH99] C. Levin and J. Hoffmann. *Phys. Med. Biol.* **44** (1999) 781.

[Mat88] E. Mathieson. *Nucl. Instr. and Meth.* **270** (1988) 602.

[Mel66] A. Melissinos. *Experiments in Modern Physics*. Academic Press, New York, 1966.

[MF84] E. Mathieson and J. Fordon. *Nucl. Instr. and Meth.* **227** (1984) 267.

[MRRS85] G. Musiol, J. Ranft, R. Reif et al. *Kern- und Elementarteilchenphysik*. VCH, 1985.

[Nat86] F. Natterer. *The mathematics of computerized tomography*. siam, 1986.

[NK29] Y. Nishina and O. Klein. *Phys. Zeit.* **52** (1929) 853.

[Nol89] W. Nolting. *Grundkurs Theoretische Physik 3 Elektrodynamik*. Vieweg, 1989.

[OLS$^+$93] I. Orlic, K. Loh, C. Sow et al. *Nucl. Instr. and Meth.* **B74** (1993) 352.

[Pie08] J. Pietschmann. *Development of a Novel Readout System for Small Animal Positron Emission Tomography*. Diplomarbeit, Institut für Kernphysik, 2008.

[Sau77] F. Sauli. CERN, CERN, Geneva, 1977 92 p, 92 p. CERN, Geneva, 1975 - 1976.

[Sch09] K. Schäfers. *private communication*, 2009.

[Smi99] L. Smith. *An investigation into limits of resolution in Positron Emission Tomography resulting from non-collinear positron annihilation*. diploma thesis, University of Melbourne, 1999. `http://www.ph.unimelb.edu.au/photo/people/leighton/thefinalcheck.pdf`.

[WA04] M. N. Wernick and J. N. Aarsvold. *EMISSION TOMOGRAPHY, The Fundamentals of PET and SPECT*. Elsevier Inc., 2004.

Danksagung

Hiermit danke ich allen Personen, die mich in den letzten Jahren unterstützt und zum Gelingen dieser Arbeit beigetragen haben.

Vor allem danke ich Prof. Dr. Johannes P. Wessels für die Aufnahme in die Arbeitsgruppe, die Möglichkeit meine Diplomarbeit im Projekt Small Animal PET schreiben zu dürfen und die Rahmenbedingungen für eine produktive und kompetente Arbeitsgruppe geschaffen zu haben. Auch möchte ich mich dafür bedanken, dass ich an der European Summer University 2008 in Strassburg, der MPGD Konferenz 2009 in Kolympari und der FANTOM week in Emmen teilnehmen durfte.

Vor allem möchte ich mich bei Holger Gottschlag für die intensive Betreuung und das lockere Arbeitsklima im Büro danken.

Ein großer Dank geht an Thomas Kösters, Dr. Klaus Reygers, Jan Frederick Pietschmann, Dr. Christian Klein-Bösing, Dr. Tom Dietel, Prof. Dr. Alfons Khoukaz und Dr. Klaus Schäfers für die zahlreichen Diskussionen, Kritiken und Ideen, ohne die diese Arbeit nicht zustande gekommen wäre.

Desweiteren möchte ich mich bei Sebastian, Björn, Henriette, Mattias, Holger, Christoph, Jan, Bastian, Markus, Simon, Cyrano, Jonas, David, Markus, Matus, Melanie, Christian, Stefan, Michael, Manuel, Friederike, Baldo, Prof. Santo, Prof. Eva, Anton, Mattias, Uwe und Alex für das nette Arbeitsklima in der Arbeitsgruppe und für die vielen nützlichen Hilfen bedanken.

Außerdem will ich mich auch bei Norbert Heine, Roland Berendes, Wolfgang Verhoeven, Helmut Baumeister, Vladimir Buglak, Georg Bourichter und Georg Hackmann für die Fertigung der von mir gewünschten mechanischen und elektrischen Apparaturen und dem Lösen der vielen technischen Probleme bedanken.

Meine größte Wertschätzung gilt natürlich den Menschen, die mir das vielfältige Leben neben der Physik verschönern. Meiner Freundin Jutta danke ich für die wunderbaren Jahre, die wir bislang miteinander verbringen durften.

Meinen Eltern und meiner Schwester danke ich für die bedingungslose Unterstütung an der es seit meiner Geburt nie gefehlt hat.

Zuletzt möchte ich noch meinen Freunden dafür danken, dass sie es immer wieder geschafft haben mich von der Physik abzulenken.

Eigenständigkeitserklärung

Hiermit bestätige ich, dass ich diese Arbeit selbstständig verfasst und keine anderen als die angegebenen Quellen und Hilfsmittel verwendet habe.

Münster, 24. Dezember 2009

Don Vernekohl